Cycle 4 Photometric Calibration of the Faint Object Spectrograph

R. C. Bohlin, D. J. Lindler, C. D. Keyes
July 1995

ABSTRACT

The cycle 4 absolute photometric calibration of the Faint Object Spectrograph is derived from observations of eight spectrophotometric standard stars, including four white dwarf (WD) stars with pure hydrogen atmospheres, in the 4.3" square and 1" circular entrance apertures for 14 detector-disperser combinations (six for the blue digicon, and eight for the red). Except for red G190H and red G160L, the observations of the eight stars over the period of February 1994 through July 1995 show no systematic variation in the sensitivity with time.

During the period from February 1994 through July 1994, a ~2 percent drop in sensitivity for the red G190H mode is evident. However, from the period of July 1994 through July 1995, the red G190H sensitivity increases by 3 to 8 percent. The red G160L behaves similarly below 2200Å.

Changes in the FOS flux calibrations relative to those in use by the pipeline since 1994 March 21 are typically less than ~3% in high dispersion for the 4.3" (A-1) and the 1" (B-3) apertures and exceed 10% only in small regions for the low dispersion modes. Small aperture fluxes differ by over 10% shortward of 1300Å for the 0.3" (B-2) aperture, since the transmissions of the small apertures were not measured until after 1994 March.

The residuals of the FOS fluxes in comparison to the WD pure hydrogen model atmospheres are less than ~2% in high-dispersion and provide the best measure of small scale errors in the FOS fluxes. The overall uncertainty of the FOS flux calibration for point sources is estimated to be 3%.

1. INTRODUCTION

Each spectrographic mode has an absolute calibration, i.e., sensitivity (S) that can be used to derive the flux of a point source as a function of wavelength by $F = C / S$, where F is the flux of the source and C is the observed counts per second. S can be calculated from the count rates of spectrophotometric stars with known fluxes (see section 3) as:

$$S = C / F \quad (1)$$

All observations discussed in this report were obtained in the A-1 (4.3") or the B-3 (1.0" circular) apertures. The aperture transmissions for point sources (Bohlin and Colina 1995) define calibrations for the 1" (B-3) and other small apertures relative to the 4.3" aperture flux calibrations. With the exception of the red prism, the complete set of cycle 4 FOS calibration data is robust enough to characterize the time changes and to determine mean calibrations that are internally consistent to better than 2% for the more photometric high dispersion modes.

In practice, the uncertainties in an individual observation stem from low counting statistics, from uncertain dark count subtraction, from pointing errors, from light scattered off the gratings, and from scatter in the positioning of the spectrum on the FOS diode array. The calibration data for the eight bright calibration standard stars do not suffer from the first three of these possible errors, because of high signal levels and peak-up target acquisitions that are accurate to 0.026 arcsec in each axis. Since the installation of the COSTAR optics, the effect of OTA focus errors on FOS photometry has become negligible.

2. FOS DATA PREPARATION

The IDL testbed version of the standard FOS pipeline reduction routine, CALFOS, is used to uniformly process each individual cycle 4 calibration observation with the most recent calibration files. This standard processing includes the following steps, which produce the net count rates that are required for sensitivity computation. The cycle 1 through 3 pre-COSTAR FOS calibration of Lindler & Bohlin (1994) followed the same prescription, except that the GIMP correction is now done in the instrument, rather than by ground software.

1. Conversion to count rates. The raw .d0* counts are corrected for the dead diodes and converted to true count rates (Lindler & Bohlin 1988).
2. Background subtraction. A particle background and dark rate is subtracted using a background model that varies with geomagnetic latitude (Lyons et al. 1992).
3. The flat field correction uses the flat fields currently installed in PODPS by Keyes and decouples the flat field effects from the absolute calibration, according to the procedure of Lindler et al. (1993).
4. Residual background and scattered light is subtracted for the modes which include a wavelength region where the response to the dispersed light is zero. The

scattered light correction is especially important in computing the calibration in wavelength regions of low sensitivity. As the sensitivity approaches zero, the scattered light becomes a large fraction of the observed light. The scattered light estimate is the average count rate in regions of zero sensitivity (Kinney and Bohlin 1993).

5. Wavelengths are computed using the dispersion coefficient table presently used by PODPS (Kriss, Blair, and Davidsen 1991).

6. In order to monitor for possible photometric error associated with the centering of the spectra on the diode array in the direction perpendicular to the dispersion, data are collected for each observation at three different y-deflections of the diode array, one at the nominal y-position and two offset by 0.156 arcsec above and below the nominal position. The count rates for the lower and upper y-steps are normalized to the center y-step, and all three spectra are averaged.

3. SPECTROPHOTOMETRIC STANDARD STARS

Uncertainty in the absolute flux F of the standard stars was the dominant error in previous FOS absolute flux calibrations. Random photometric errors and systematic uncertainties are present in the previous reference standards, which are composed of IUE fluxes in the UV (Bohlin et al. 1990) and ground based spectra from Oke (1990) in the visual. Since all FOS wavelengths are measured in vacuum, the Oke wavelengths are transformed from air to vacuum values. Photometric errors are typically a few percent and range up to 10% in the difficult region for both IUE and Oke around 3200Å, while the absolute IUE flux scale is low by 5-10% in the UV in comparison to models for pure hydrogen white dwarfs (WD).

Now, all the FOS flux standards are pure hydrogen WD models or are based on FOS photometry relative to the WD G191B2B, as detailed in Lindler & Bohlin (1994). Absolute flux distributions for the four WD models appear in Bohlin, Colina, & Finley (1995). FOS photometry relative to G191B2B establishes the fluxes for the four non-WD standards; i.e. FOS data is used as the standard below 3850Å, while the higher S/N Oke spectra are bent to the broadband FOS shape at longer wavelengths. This set of eight spectrophotometric standard stars, G191B2B (WD0501+527), BD+75°325, HZ44, BD+33°2642, BD+28°4211, GD71, GD153, and HZ43 is used for the sensitivity calibration of the FOS.

To summarize the current status of the standard star spectrophotometry, the external accuracy of the absolute flux scale is determined by how well the G191B2B model predicts the actual stellar flux distribution and is estimated to be within about 3% of the truth in the UV after normalizing to the Landolt visual photometry (Bohlin, Colina, & Finley 1995). Since the differences between the FOS absolute photometry for the average spectra of these eight stars and Landolt (1992 & private communication) B and V photometry show an rms scatter of less than 1% (cf. Colina and Bohlin 1994), both the Landolt data and the FOS spectra are excellent photometry. See Bohlin (1995) and Lindler & Bohlin (1994) for more

details. For a normal FOS science observation of a point source, the accuracy of absolute fluxes is limited by the uncertainties in the observation itself and not by uncertainties in the flux calibration files.

4. SENSITIVITY COMPUTATION

A raw sensitivity curve is computed for each observation by taking the ratio of the processed count rate divided by the star's reference flux distribution for each of the individual cycle 4 observations, as summarized by star and FOS mode in Table 1. For all dispersers except the prism, the observed FOS count rate and the reference flux distribution are rebinned using trapezoidal integration to a common wavelength scale with 5Å bins or 6 FOS pixels, if 6 px is greater than 5 Å. For the prism, the standard star spectrum is rebinned using trapezoidal integration over the four pixel FOS diode width. Observations in the B-3 (1.0" circular aperture) are normalized to the A-1 aperture (4.3" square) using the aperture throughput functions described in Bohlin & Colina (1995).

Table 1. Number of Visits to Standard Stars for Each FOS Dispersion Mode

Detector	Disperser	G191-B2B	BD+75° 325	HZ44	BD+33° 2642	BD+28° 4211	GD153	GD71	HZ43
BLUE	H13 (G130H)	4	1	1	1	6	3	2	3
BLUE	H19 (G190H)	3	1	1	1	6	3	2	3
BLUE	H27 (G270H)	3	1	1	1	7	3	2	3
BLUE	H40 (G400H)	3	1	1	1	6	3	2	3
BLUE	L15 (G160L)	4	1	1	1	6	0	0	0
BLUE	PRISM	2	0	1	0	6	0	0	0
RED	H19 (G190H)	4	1	0	1	7	3	2	3
RED	H27 (G270H)	4	1	0	1	4	3	2	3
RED	H40 (G400H)	3	1	0	1	6	3	2	3
RED	H57 (G570H)	3	1	0	1	6	3	2	3
RED	H78 (G780H)	2	1	0	1	6	3	2	3
RED	L15 (G160L)	4	1	0	1	6	0	0	0
RED	L65 (G650L)	2	1	0	1	6	0	0	0
RED	PRISM	2	0	0	0	5	0	0	0

A least squares cubic spline is fit to the logarithm of the raw sensitivity curves to generate a smooth sensitivity curve. Table 2 lists the regions on the red digicon with photocathode blemishes that have not yet been adequately removed by flat fielding and the regions on both detectors with strong spectral lines. These excluded regions are masked in the fitting

process; and the spline fits across these gaps can be potential sources of spurious wiggles at the 1-2% level in the sensitivity fits. Therefore, new sensitivity curves should be generated whenever there are upgrades to the flat field corrections.

Table 2. Regions Excluded From the Sensitivity Computation

Wavelength Region (Å)	Dispersive Mode of Star	Reason
1200 - 1232	all stars	L-α Geocorona
1545 - 1555	G191B2B	CIV not in model
2790 - 2810	G191B2B	MgII not in model
3950 - 4000	all stars	Strong H-ε
4075 - 4125	all stars	Strong H-δ
4310 - 4370	all stars	Strong H-γ
4810 - 4910	all stars	Strong H-β
6500 6620	all stars	Strong H-α
1922 - 1943	Red G190H	Changing FF
2295 - 2330	Red G270H	Changing FF
2573 - 2595	Red G270H	Changing FF
8300 - 8400	Red G780H	Strong FF spike

The number of spline nodes used in each disperser mode is given in Table 3. An asterisk indicates that unequally spaced nodes are used. In these cases, nodes are placed at specific wavelengths to follow better the curvature of the sensitivity function.

Table 3. FOS Modes and Number of Spline Nodes

Detector	Disperser	Nodes	WL Range (Å)
BLUE	H13 (G130H)	17 *	1140 - 1606
BLUE	H19 (G190H)	28 *	1573 - 2330
BLUE	H27 (G270H)	20	2221 - 3301
BLUE	H40 (G400H)	18	3240 - 4822
BLUE	L15 (G160L)	26 *	1140 - 2508
BLUE	PRISM	30 *	1500 - 5959
RED	H19 (G190H)	28 *	1590 - 2312
RED	H27 (G270H)	20	2222 - 3277
RED	H40 (G400H)	18	3235 - 4781
RED	H57 (G570H)	15	4569 - 6818
RED	H78 (G780H)	10	6269 - 8499
RED	L15 (G160L)	25 *	1571 - 2424
RED	L65 (G650L)	23 *	3540 - 7075
RED	PRISM	31 *	1620 - 8887

The average sensitivity curves are shown in Figure 1. In the case of G160L blue, the wavelength range in Table 3 is more than a factor of two, so that there is contamination of the first order longward of ~2300Å by second order light. Quantitative estimates of this problem are provided by FOS sky spectra, which have a count rate due to second order Lyman-alpha of about one-half of the first order count rate. For a continuum source, the doubling of the dispersion in second order causes a drop in the relative contamination by another factor of two. The relative sensitivity to a continuum source at 1216Å vs. 2432Å is a factor of 48, so that for a flat continuum source (F(λ)=constant), the first order light contamination at 2432Å is only ~0.5% and has been ignored in the G160L calibration results. For our hottest stars, the continuum is not flat but rises by a factor of 6 from 2400 to 1200Å, so there would be ~3% contamination by second order light at 2432Å.

5. TIME VARIATIONS OF THE SENSITIVITY

Unlike the sensitivity calibration for cycles 1-3 (Lindler & Bohlin 1994), there is no significant variation in sensitivity with time, except for the red side G190H and G160L gratings (Figure 2). From the period of February 1994 through July 1994, red G190H shows ~2% loss of sensitivity, which is followed by a gain in sensitivity of up to 8% in the 1900-2000Å region during the period of August 1994 to July 1995. The models for the red

G190H and G160L corrections evaluated at 0.3 year intervals are shown in Figure 3. Except for red G190H and G160L, the pipeline processing will use the average sensitivity curve with no time corrections for FOS observations taken after the first HST servicing mission in 1993 December.

6. ERROR ANALYSIS

Figure 4 shows the rms deviation versus wavelength of the individual sensitivity curves from the average sensitivity curve for each dispersive mode. Table 4 gives the average rms photometric scatter for each mode. These rms deviations in the individual sensitivity curves are an indication of the photometric accuracy that may be achieved for an arbitrary GO observation.

Table 4. Percent rms Scatter in the Sensitivity Curves Averaged Over All Wavelengths for Each Mode

Detector	Disperser	Cycles 1-3	Cycle 4
BLUE	G130H	1.8	1.6
BLUE	G190H	1.6	1.3
BLUE	G270H	1.1	0.9
BLUE	G400H	1.5	0.8
BLUE	G160L	2.2	1.8
BLUE	PRISM	3.4	1.8
RED	G190H	2.0	1.3
RED	G270H	1.2	0.9
RED	G400H	1.2	0.8
RED	G570H	1.2	0.6
RED	G780H	1.3	1.2
RED	G160L	3.4	2.4
RED	G650L	3.0	1.6
RED	PRI	4.7	2.4

In a few cases, large photometric errors (greater than 3 σ) are found in the observations. Table 5 gives a list of the observations of the standard photometric sources that were deleted from our analyses of repeatability.

Table 5. Observations Deleted from this Analysis

Proposal	Rootname	Detector	FGWA_ID	Aperture	Target	Date	Reason
5539	y2et020jt	RED	H27	B-3	BD28	6/30/94	Bad Y-base
5539	y2et020kt	RED	PRI	B-3	BD28	6/30/94	Bad Y-base
5539	y2et0210t	RED	H27	A-1	BD28	6/30/94	Bad Y-base
5539	y2et0e0xt $x = 5$ to c	RED	all	B-3	HZ44	4/3/95	T/acq err?

The three red side observations with the Y-base problem represent 2.4% of all of the red side standard star observations and are all low by 2-4% in flux. On the red side, the proper Y-base for an FOS observation is difficult to determine precisely because of a one sigma scatter of ~0.1" in the measurements and a systematic change with time (Koratkar, Keyes, & Holfeltz 1995). Red side Y-base errors greater than 0.2" can be expected for ~10% of red side observations. However, the three red side observations with low flux must have had a total Y-base error of ~0.4-0.5" and imply an unfortunate loss of flux in a few percent of FOS observations when non-optimal commanded Y-base values, GIMP, and filter grating wheel errors combine at their maximum positional uncertainty range. For typical GO observations, larger acquisition errors of ~0.2" combine with non-optimal Y-base positioning of the spectrum on the diode array to cause more frequent photometric problems.

The entire set of red side observations of HZ44 are low in flux by 5-10% and have not been included in the calibration data for FOS. An examination of the target acquisition data suggests that the initial pointing error exceeded 2" and prevented the peakup sequence from converging exactly. Zero proper motion was entered, while Luyton and Miller (1951) give -0.052 and +0.035 arcsec/yr on the sky for the proper motion in right ascension and declination, respectively. Since HZ44 may be at a distance of 1-2 kpc, this value of proper motion might be treated as an upper limit. However, in the 11 years since the 1984 epoch of the Guide Star plate, HZ44 may have moved a significantly large 0.7". The actual direction of the initial FOS pointing error and the earlier epoch Palomar plate positions should be checked to independently estimate proper motion for HZ44.

7. WHAT IS THE PHOTOMETRIC PRECISION OF THE FOS CALIBRATION

The overall uncertainty in the absolute FOS flux calibration is estimated at ~3%, which is a ~2 σ value derived from the combination of a 1-2% uncertainty in the model WD flux slopes, a fraction of a percent uncertainty in the Landolt photometry used to normalize the models to absolute flux, and a 1-2% internal FOS photometric repeatability (Bohlin 1995). The internal consistency is demonstrated to be better than ~2% by Figure 5, which shows

the residuals of the sum of all FOS cycle 4 observations in comparison to the standard stars on the WD scale. For a case where the model flux distributions are used as the standard, the high S/N co-added spectrum for G191B2B has residuals of <2% in high dispersion on all wavelength scale-lengths, except in the spectral lines, where small wavelength errors and resolution mismatches can cause bigger problems. The G780H region is somewhat worse because of lower S/N and more uncertainty in the flats. The low dispersion modes are less photometric, especially for the prisms and at the Balmer lines, where the resolution is badly mismatched. Actual FOS observations of point sources may have more uncertainty than the 3% associated with the calibration files, especially if the pointing uncertainty exceeds 0.1-0.2 arcsec.

8. WHAT IS THE TYPICAL PHOTOMETRIC PRECISION FOR AN INDIVIDUAL OBSERVATION?

The individual observations of the eight standard stars provide statistics of the photometric precision of the FOS. Table 4 summarizes the broadband repeatability, while Figure 6 illustrates the repeatability graphically for a 5Å wavelength bin size. Individual observations of the four WD standards are ratioed to the WD models in the UV, where the only confusing spectral feature in the denominator spectrum is L-α. Except for the high S/N and for the target acquisition precision of 0.026" in each axis, these observations should be typical of any GO observation of an isolated point source in the larger FOS apertures. There are some 3% features of up to 500Å wide in the top three panels of Figure 6a that may be attributable to changes in the photocathode or to small shifts of the spectrum on the detector cathode. An amazingly precise short term repeatability for observations within ~1-2 days, even with intervening separate target acquisitions, is illustrated by the ratios in the top two panels of both Figure 6a and 6b. The first two observations of G191B2B include the data that determine the flat field correction and are at a typical S/N of greater than 200 per 5Å bin, while the remainder of the data have S/N greater than about 100.

Therefore, the narrow features that are bigger than ~3% must be caused by flat field misalignment or time variability, except for L-α (1216Å) in all stars and CIV (1550Å) and MgII (2800Å) in G191B2B. On the red side, dips at 1930, 2310, and 2580 that grow systematically with time from the top to the bottom of Figure 6b are due to the same changing flat field phenomenon that was present in cycles 1-3. The data exists for defining the correction to the changing flat fields and should be implemented in the pipeline by the end of August 1995. The occasional red side blips of up to ~3% at 2505Å are probably caused by misalignment of the data with the flats.

9. HISTORY OF THE CYCLE 4 FLUX CALIBRATION

The previous cycle 4 absolute calibration for FOS was implemented in the pipeline processing on 1994 March 21. This original calibration was based on only one set of observations of G191B2B and used a preliminary definition of the WD flux scale (Bohlin 1994). The differences between the fluxes for any cycle 4 data processed with the original cycle 4 calibrations and the calibrations derived here are shown for the 4.3" A-1 aperture in Figure 7, where the average is used for the time variable red G190H and G160L sensitivities. The structure in the ratios is mostly due to the preliminary WD flux corrections used in 1994 March before the model fluxes were adopted for the standard star G191B2B. Small changes in the spline nodes, additional FOS data, and updated flats also contribute to the changes. For the smaller apertures, the differences have the same shapes, because the aperture corrections are quadratic fits as a function of wavelength for each spectral mode (Bohlin and Colina 1995). For an aperture as small as the 0.3" B-2, the difference in flux exceeds 10% shortward of 1300Å, because only theoretical aperture transmissions were available in 1994 March.

The new cycle 4 calibrations derived here should be implemented in the routine pipeline processing in 1995 August. If the new calibration has been used, the header keyword AIS_CORR will be set to COMPLETED. If the changes in the FOS flux calibration described above are important for a particular science goal, then the archival data should be reprocessed. Information on obtaining FOS calibration reference files can be obtained via the world wide web with the URL identifier http://www.stsci.edu/ftp/instrument_news/FOS/topfos.html under the "ADVISORIES" topic.

10. REFERENCES

Bohlin, R. C. 1994, in Proc Conf. Calibrating HST, p234; also CAL/SCS-002.

Bohlin, R. C. 1995, STScI Instrument Science Report on Standard Calibration Sources, CAL/SCS-006.

Bohlin, R. C., & Colina, L. 1995, FOS Instrument Science Report, CAL/FOS-136.

Bohlin, R. C., Colina, L., & Finley, D. S. 1995, AJ, September.

Bohlin, R. C., Harris, A. W., Holm, A. V., & Gry, C. 1990, ApJS., 73, 413.

Colina, L., & Bohlin, R. C. 1994, AJ, 108, 1931.

Keyes, C. D., 1995, FOS Instrument Science Report, CAL/FOS-143.

Kinney, A. L., & Bohlin, R. C. 1993, FOS Instrument Science Report, CAL/FOS-103.

Koratkar, A., Keyes, C., & Holfeltz, S. 1995, FOS Instrument Science Report, CAL/FOS-133.

Kriss, G., Blair, W., & Davidsen, A. 1991, FOS Instrument Science Report, CAL/FOS-067.

Landolt, A. 1992, AJ, 104, 340.

Lindler, D. J., & Bohlin, R. C. 1988, FOS Instrument Science Report, CAL/FOS-045.

Lindler, D. J., & Bohlin, R. C. 1994, FOS Instrument Science Report, CAL/FOS-125.

Lindler, D., Bohlin, R., Hartig, G., & Keyes, C. 1993, FOS Instrument Science Report, CAL/FOS-088.

Luyten & Miller 1951, ApJ 114, 488.

Lyons, R., Baity, W., Beaver, E., Cohen, R., Junkkarinen, J., Linsky, J., & Rosenblatt, E. 1992, FOS Instrument Science Report, CAL/FOS-080.

Oke, J. B. 1990, AJ, 99, 1621.

11. FIGURE CAPTIONS

The figures accompanying this report are presented on the following pages. The descriptions of each are presented below.

Figure 1: Average Cycle 4 Sensitivity Curves for the (a) High Dispersion Modes and (b) Low Dispersion Modes. Solid lines are the blue side sensitivities, while dashed lines represent the red side results.

Figure 2: Change with Time of Sensitivity with Respect to the Averages of Figure 1. The data for three broad wavelength bins are shown and are connected by different line types. The heavy solid line is the adopted fit. Smaller symbol sizes are used to distinguish the B-3 from the A-1 aperture observations.

Figure 3: Corrections as a Function of Wavelength for a) G190H and b) G160L Evaluated Every 0.3 Year. For G190H, there is first a drop in sensitivity to a minimum around 1994.6 followed by an increase to the current maximum sensitivity. G160L shows a generally increasing sensitivity.

Figure 4: One σ rms Deviations of the Individual Sensitivity Curves from the Average Sensitivity Versus Wavelength for Each Mode. For the red G190H mode, the sensitivities are adjusted with the time model (shown in Figure 2) prior to computing the rms deviations.

Figure 5: Residual Ratios of the Co-added Spectrum in 10Å bins of Each Star Divided by the Input Standard Star Spectrum. The bin size is larger for the long wavelength portion of the prism data, where the resolution is less than 10Å. A pure hydrogen model spectrum is the standard star for the four WD's (G191B2B, GD71, GD153, and HZ43). The other four standard stars are pieced together from FOS blue, FOS red, and Oke spectrophotometry as described by Lindler & Bohlin (1994) and Bohlin (1995). The six panels in each plot are blue-red pairs of high dispersion gratings, low dispersion gratings, and prism modes, respectively. Selected broadband averages of the residuals are shown in each panel.

Figure 6: Residuals in 5Å Bins for the Individual Cycle 4 Observations of WD's, where Time of Observation Increases from Top to Bottom. Because of Geocoronal L-alpha contamination, the region around 1216Å is not shown. The broad systematic deviations of 2-3% from unity are the intrinsic limits to FOS photometric precision. However, the first two observations of G191B2B on both the blue (a) and the red side (b) demonstrate a much better repeatability that is often seen for FOS over short intervals of a few days.

Figure 7: The Changes to the Original 1994 March 21 Cycle 4 Pipeline Calibration for the 4.3" A-1 Aperture. The changes represent the ratio of the original pipeline flux in the .c1 files to a reprocessed .c1 file with the calibrations described here, except that averages over time are used for the variable red G190H and G160L sensitivities.

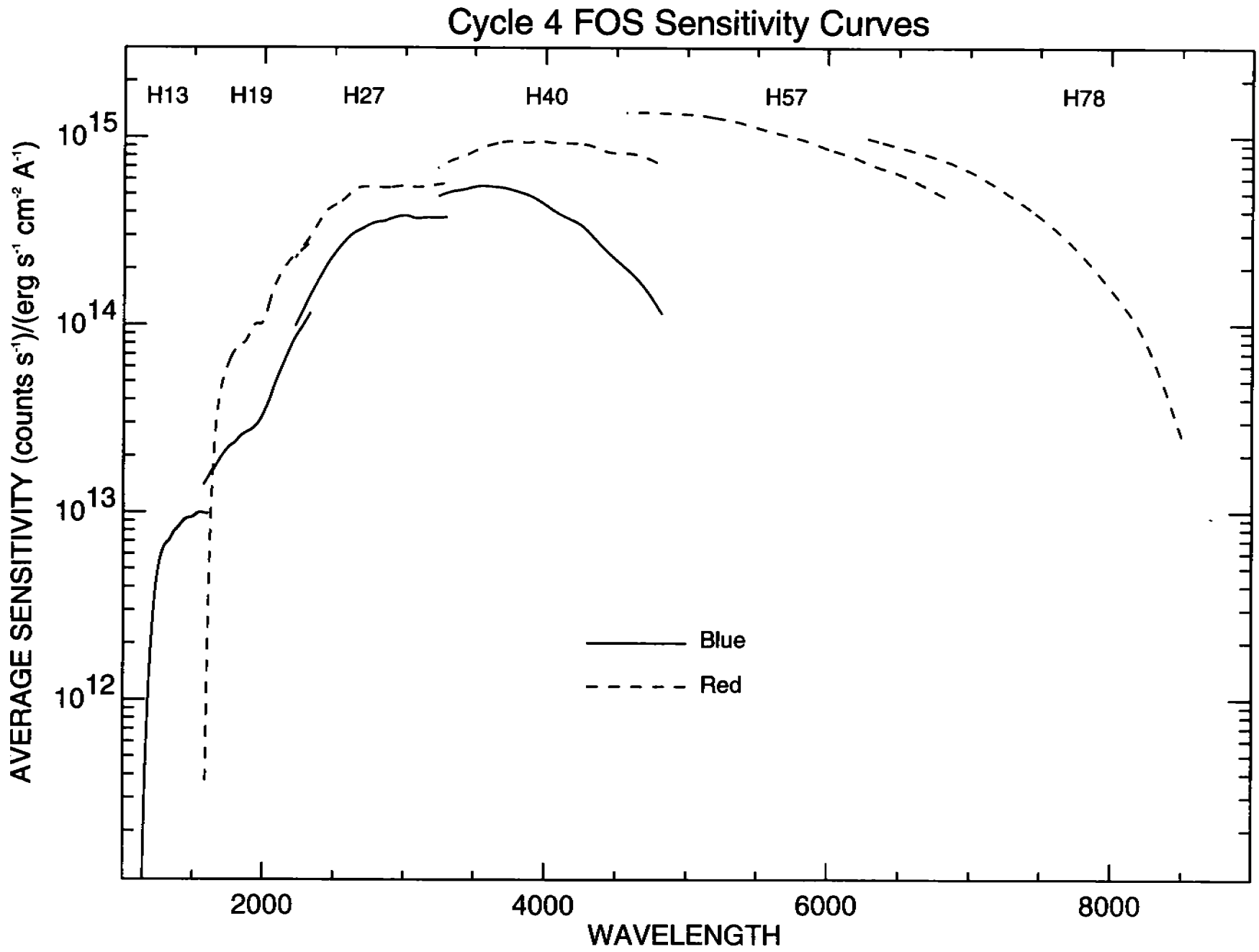
Cycle 4 FOS Sensitivity Curves
H13
H19
H27
H40
H57
H78
AVERAGE SENSITIVITY (counts s-1)/(erg s-1 cm-2 A-1)
10^15
10^14
10^13
10^12
Blue
Red
2000
4000
6000
8000
WAVELENGTH

Fig. 1a

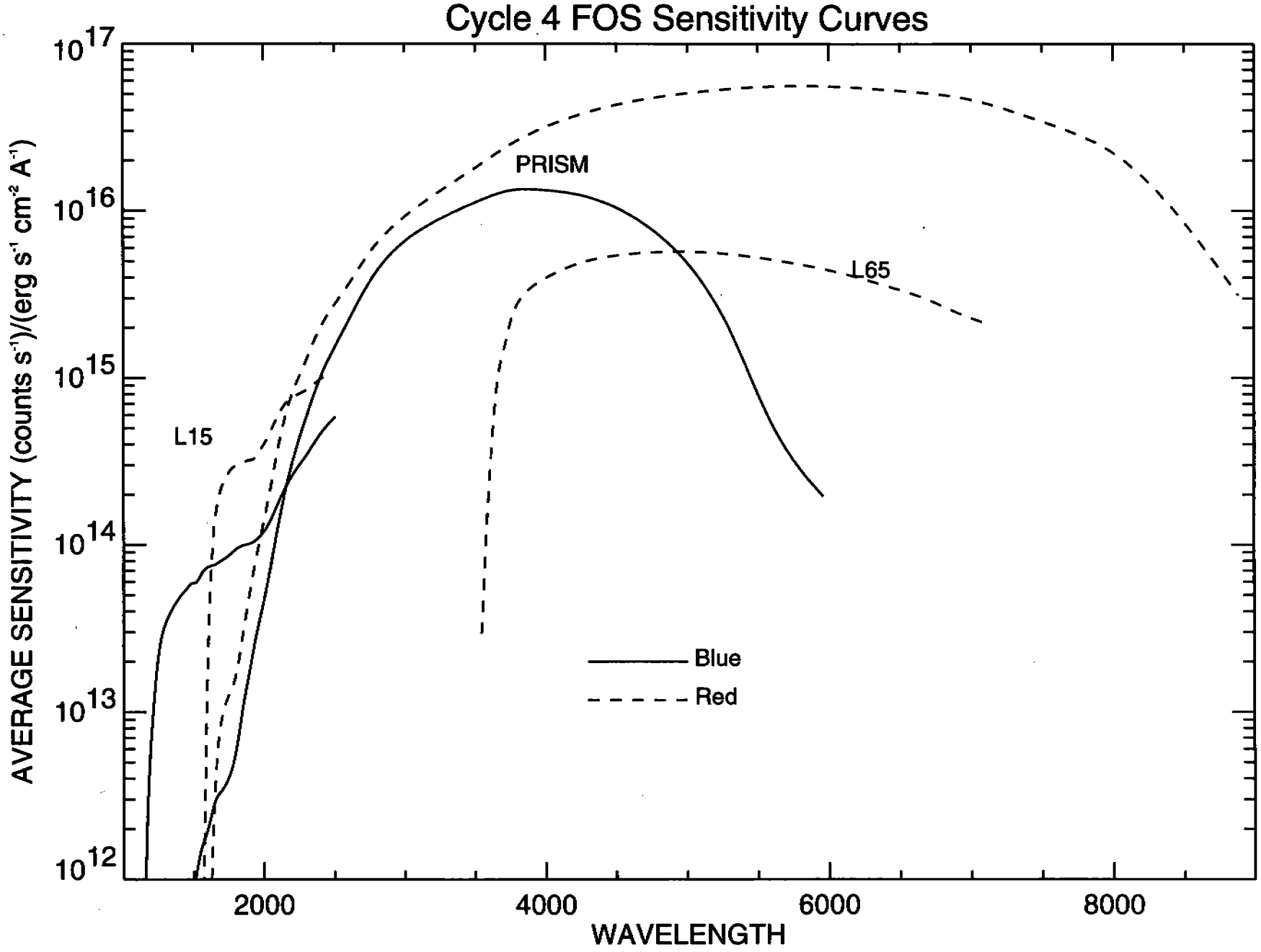
Cycle 4 FOS Sensitivity Curves
AVERAGE SENSITIVITY (counts s-1)/(erg s-1 cm-2 A-1)
10^17
10^16
10^15
10^14
10^13
10^12
PRISM
L65
L15
Blue
Red
2000
4000
6000
8000
WAVELENGTH

Fig. 1b

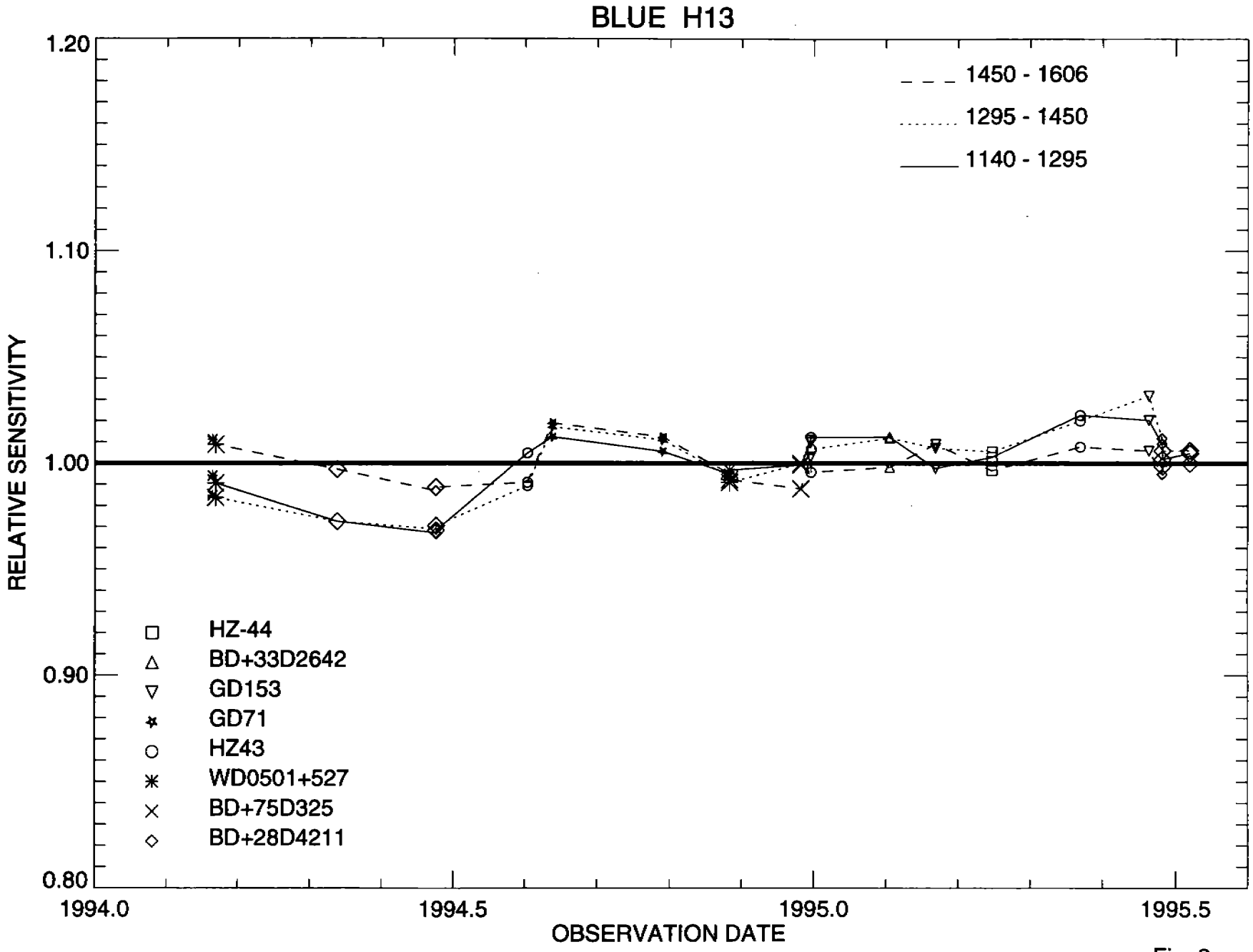

Fig. 2

LINDLER: PLTSENS_TIME 25-Jul-1995 11:22

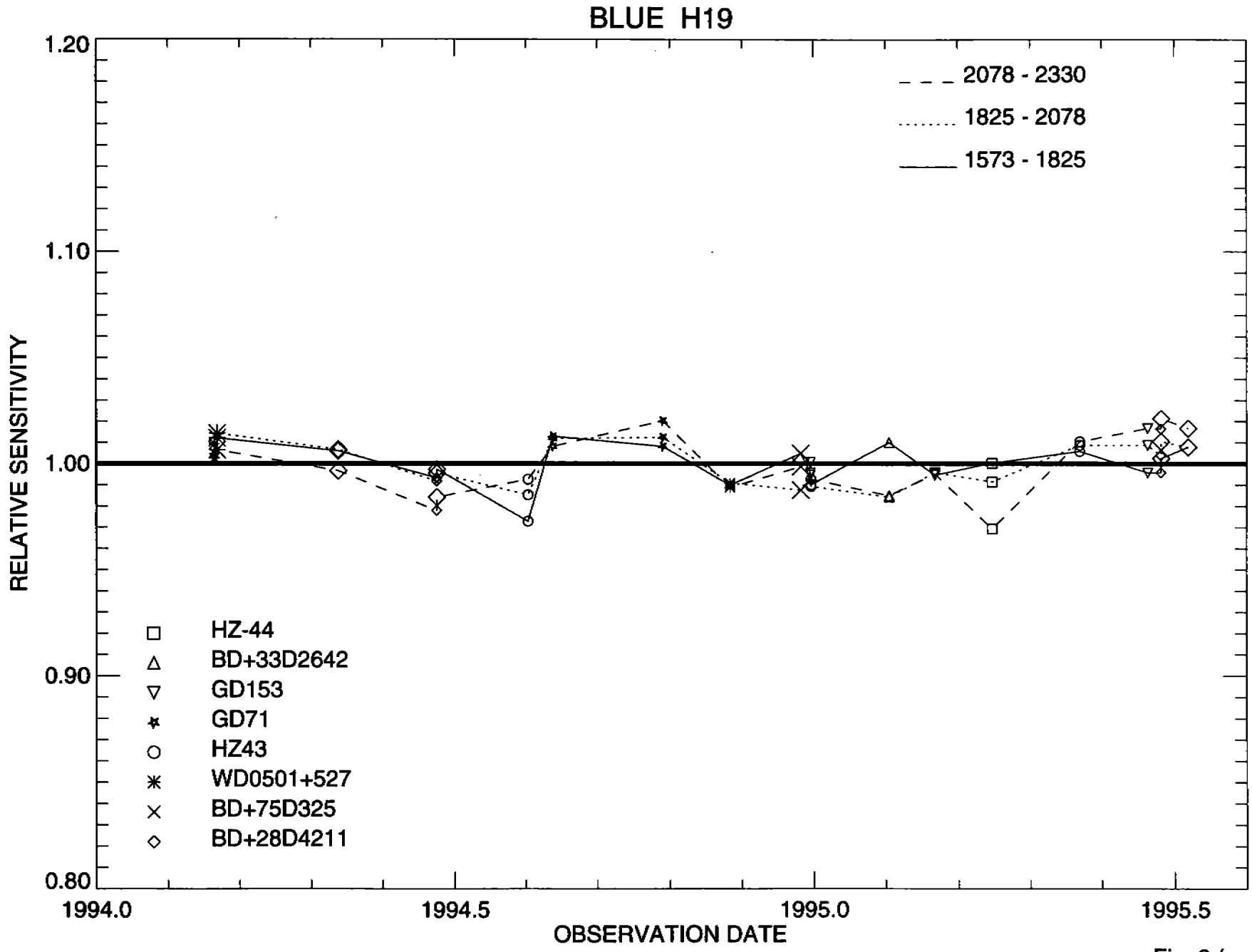

Fig. 2 (cont.)

LINDLER: PLTSENS_TIME 2[illegible]1995 11:22

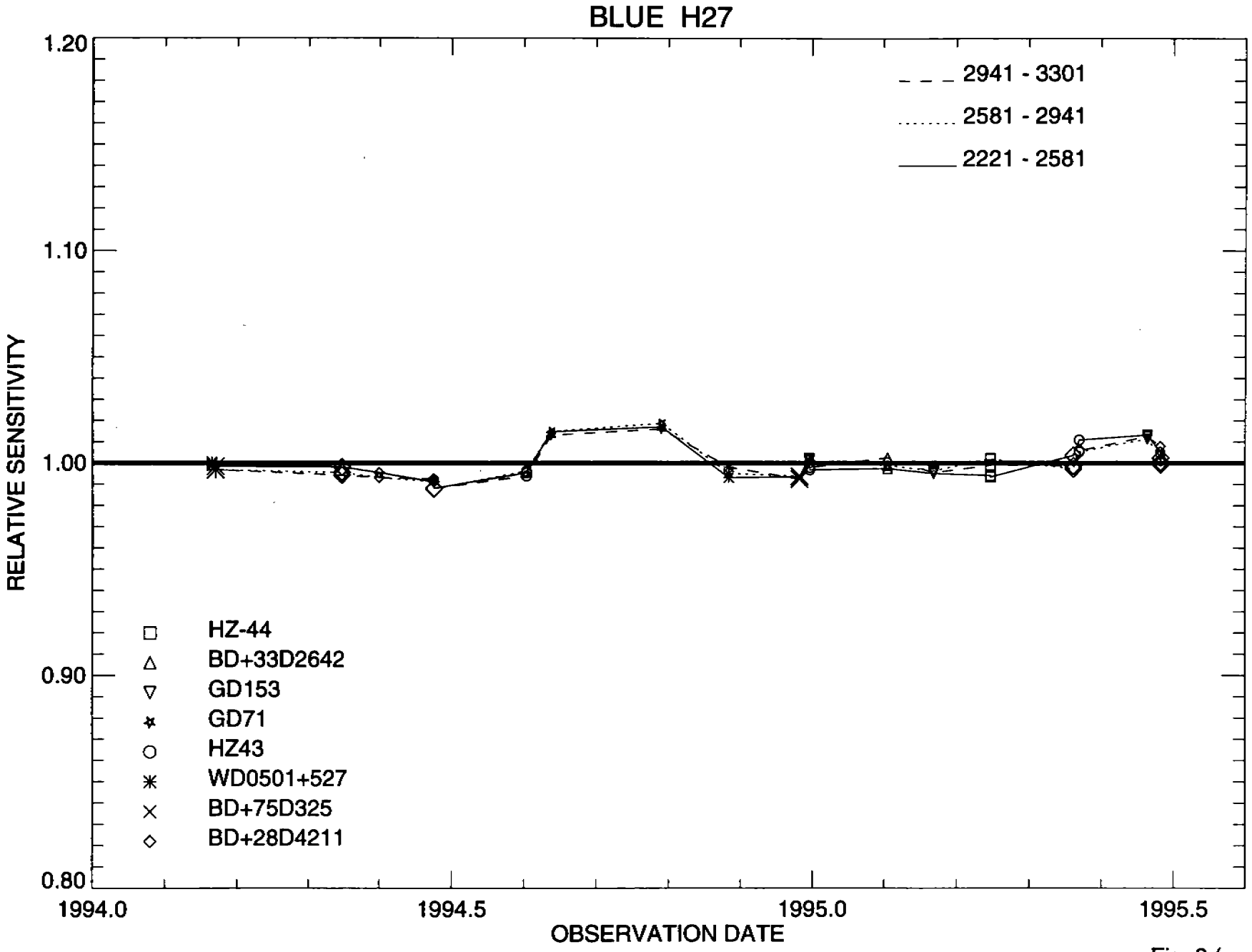

Fig. 2 (cont.)

LINDLER: PLTSENS_TIME 25-Jul-1995 11:23

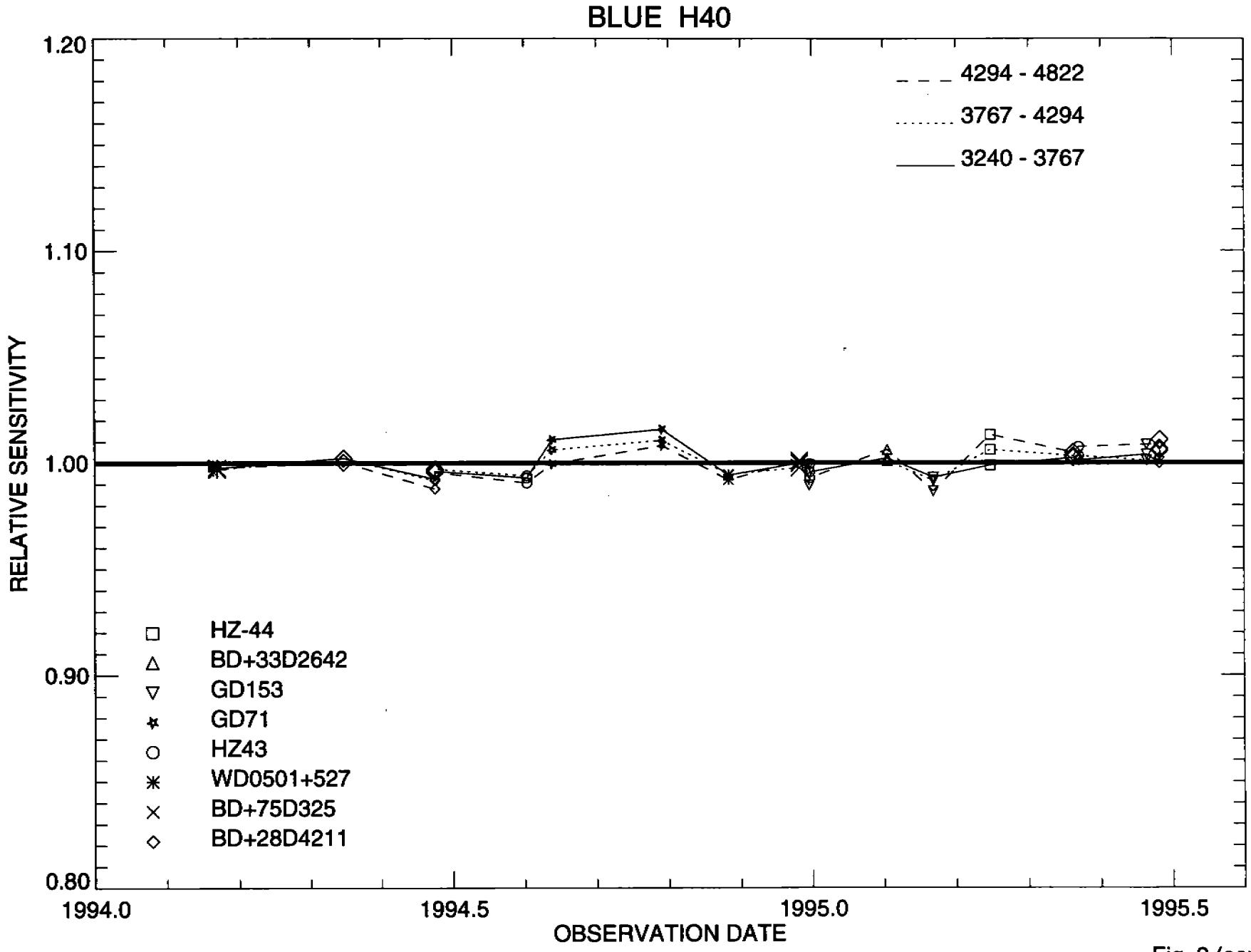

Fig. 2 (cont.)

LINDLER: PLTSENS_TIME 2[illegible]995 11:23

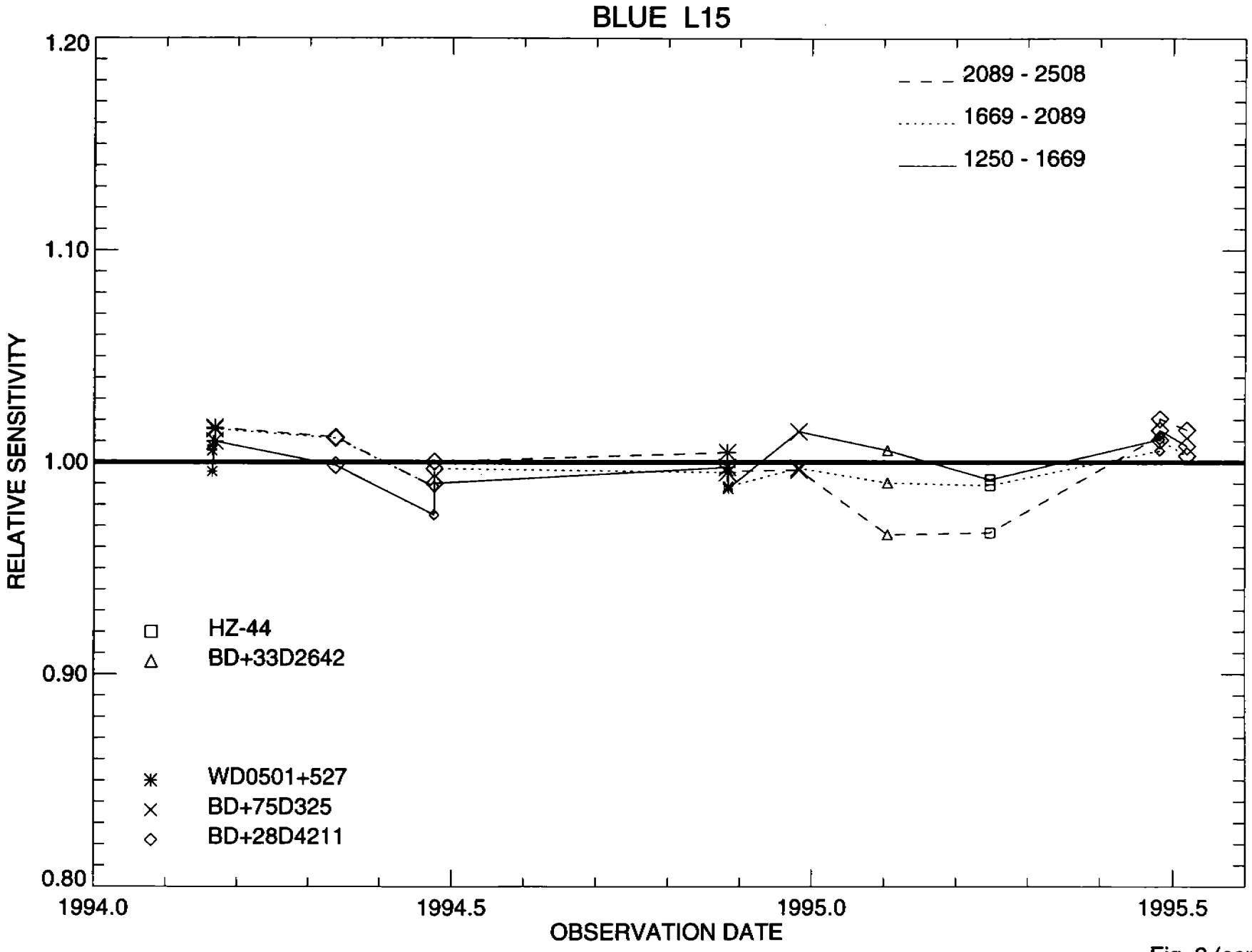

Fig. 2 (cont.)

LINDLER: PLTSENS_TIME 25-Jul-1995 11:23

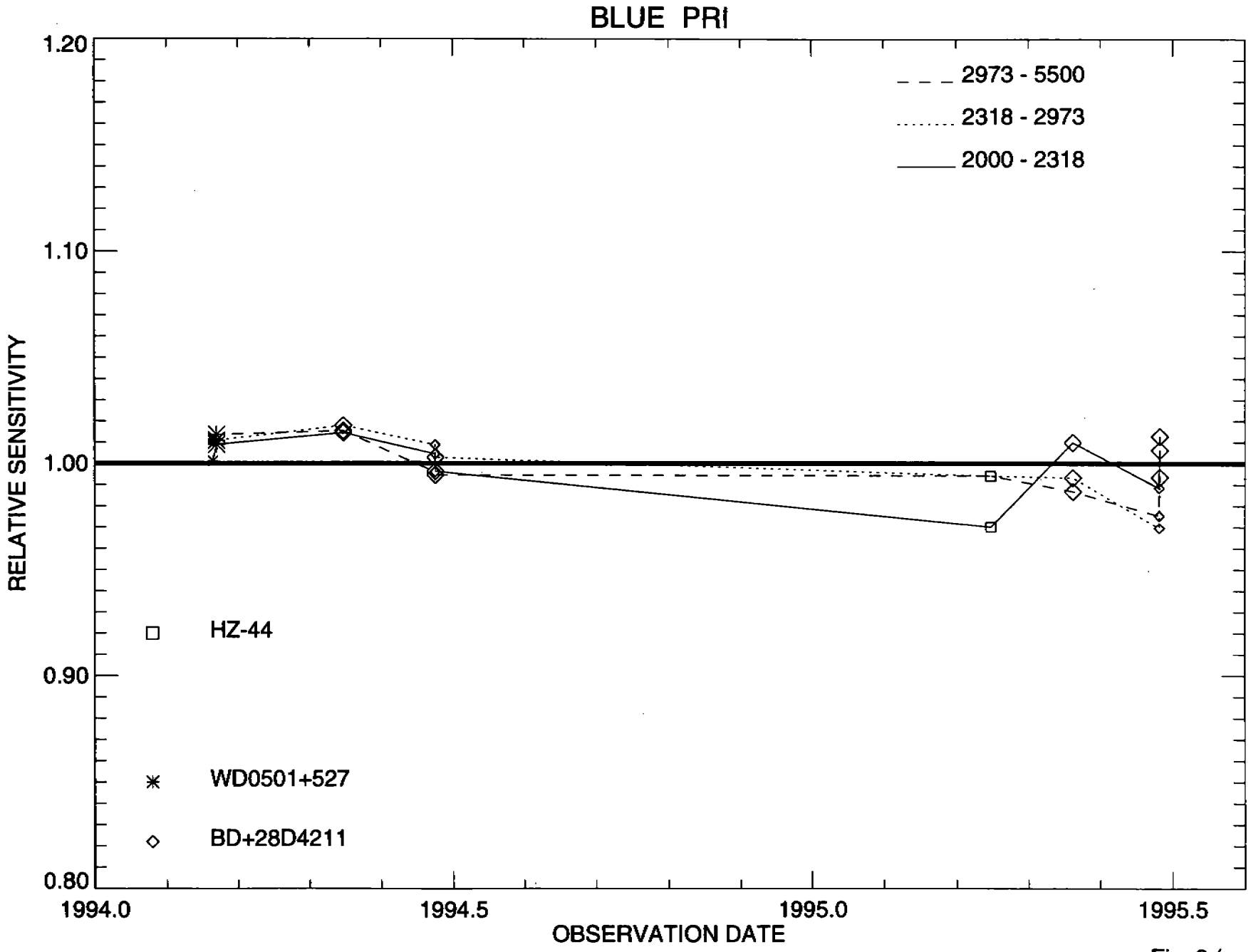

Fig. 2 (cont.)

LINDLER: PLTSENS_TIME 25 1995 11:23

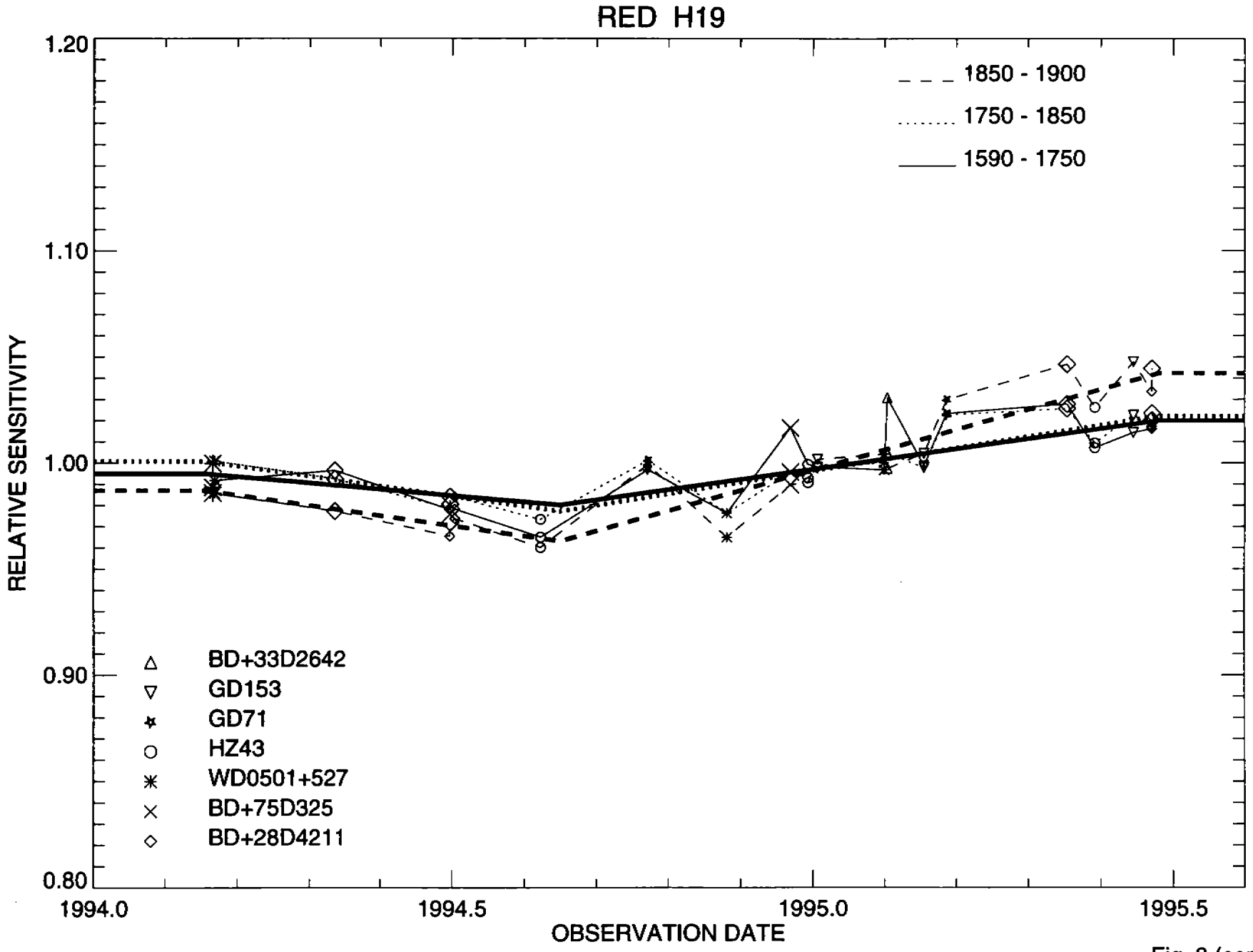

Fig. 2 (cont.)

LINDLER: PLTSENS_TIME 25-Jul-1995 11:23

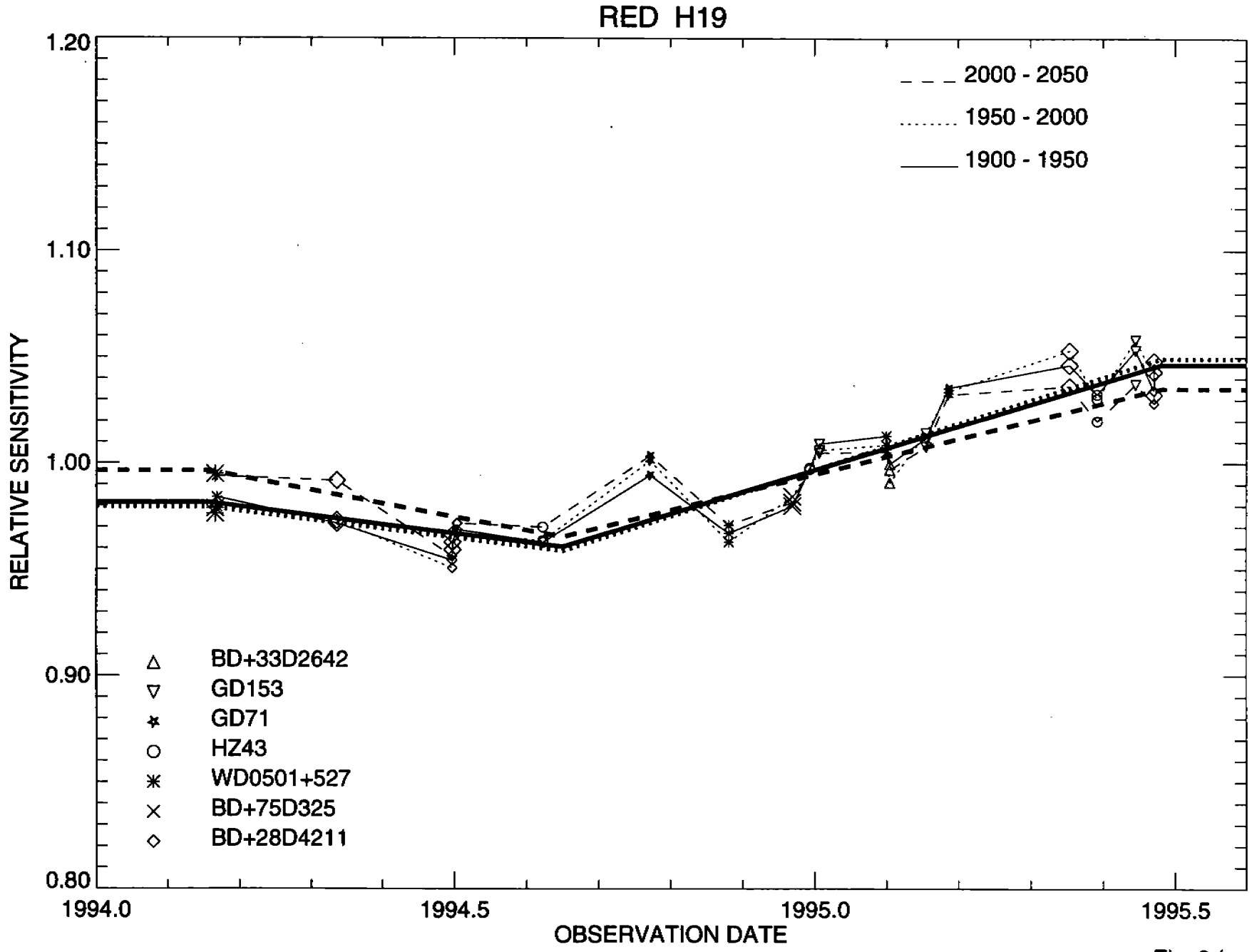

Fig. 2 (cont.)

LINDLER: PLTSENS_TIME 2[illegible]1995 11:23

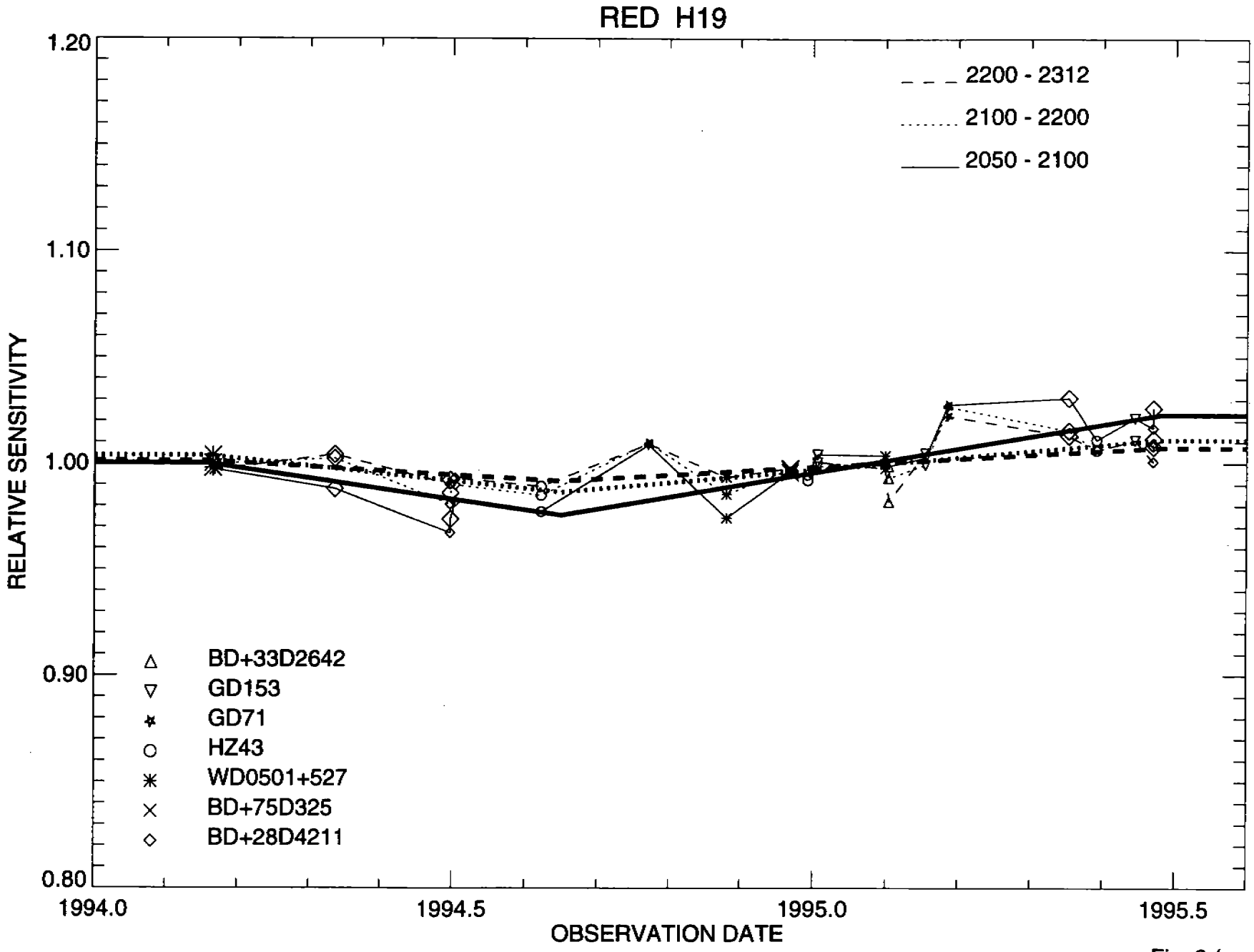

Fig. 2 (cont.)

LINDLER: PLTSENS_TIME 25-Jul-1995 11:23

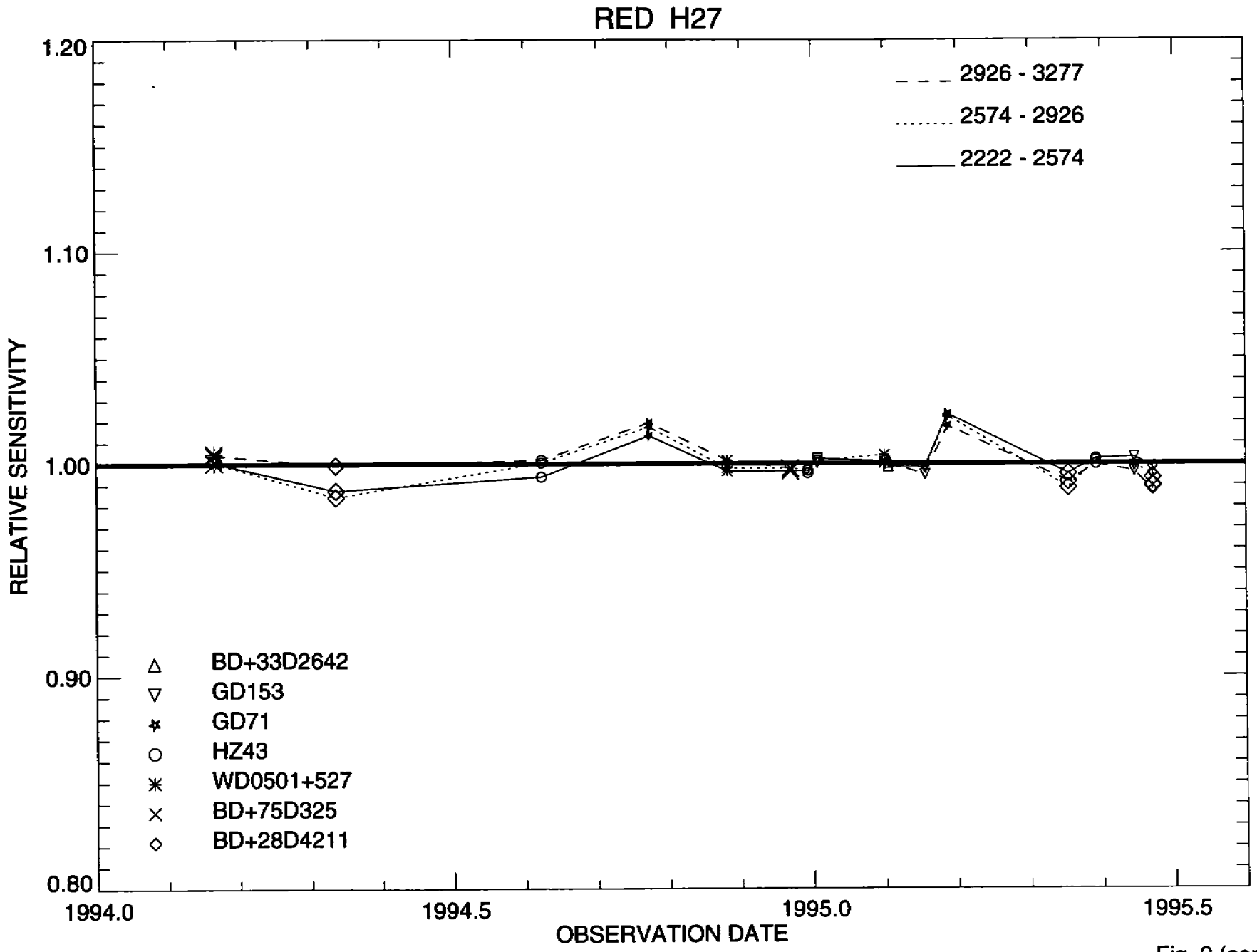

Fig. 2 (cont.)

LINDLER: PLTSENS_TIME 2 1995 11:23

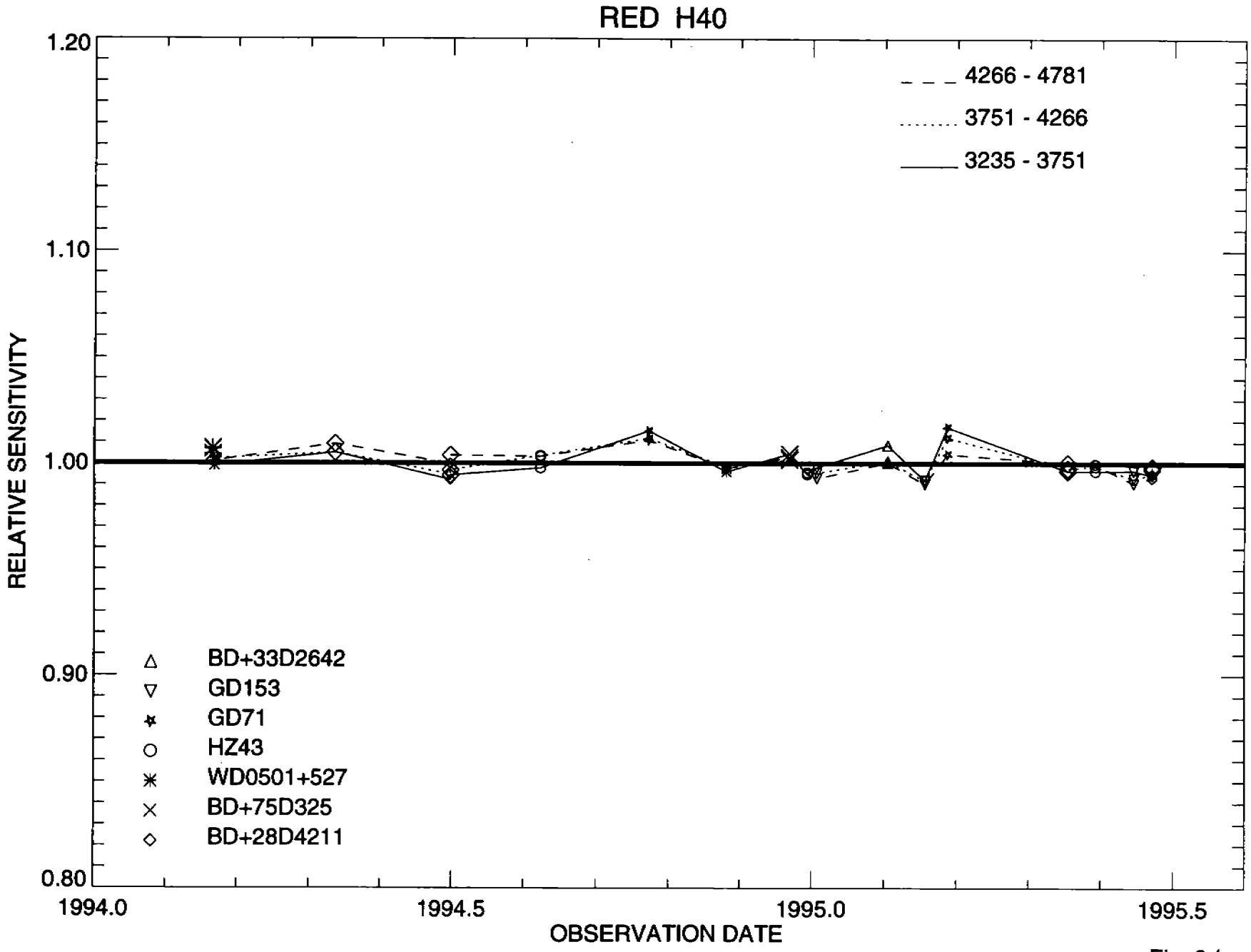

Fig. 2 (cont.)

LINDLER: PLTSENS_TIME 25-Jul-1995 11:23

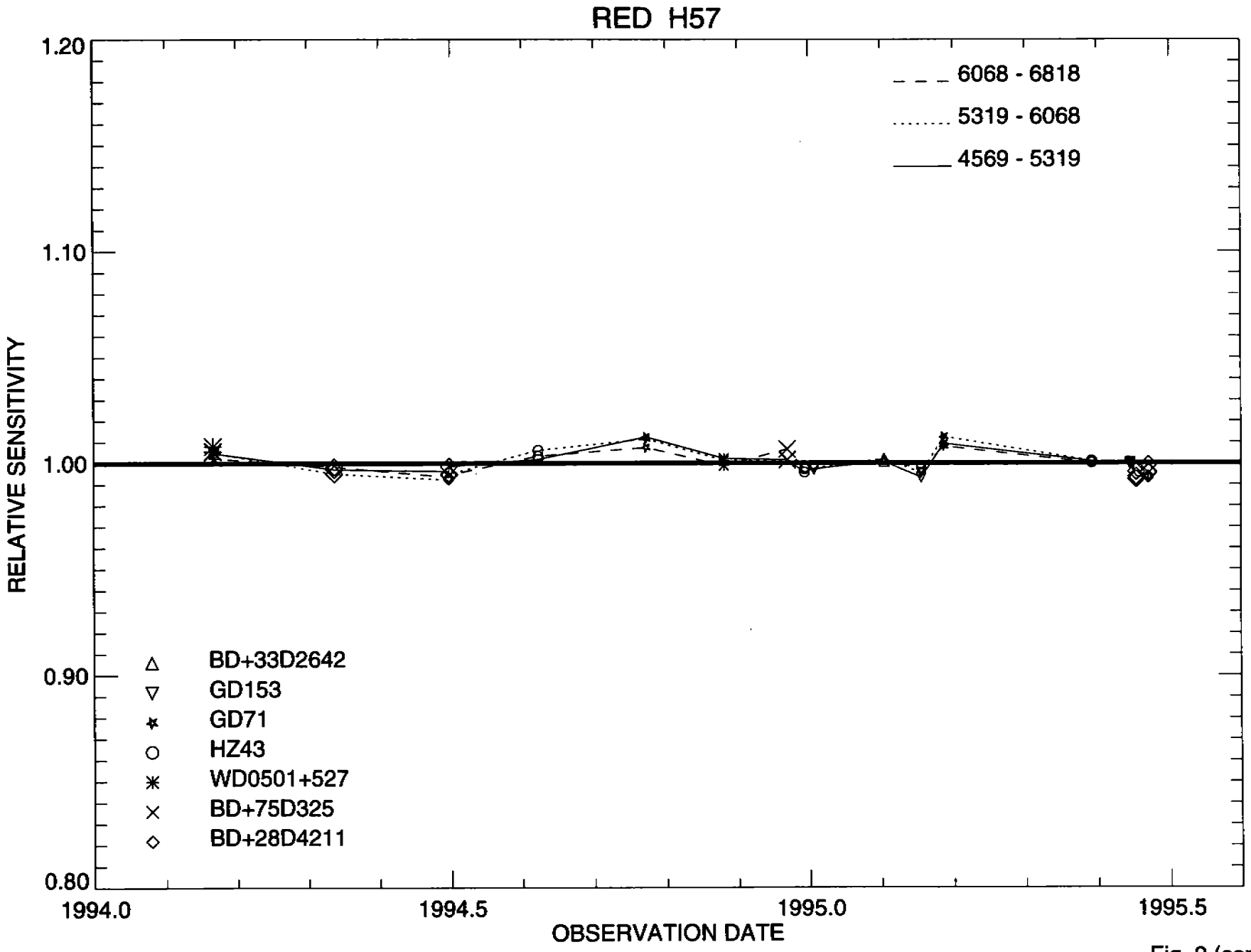

Fig. 2 (cont.)

LINDLER: PLTSENS_TIME 2 1995 11:23

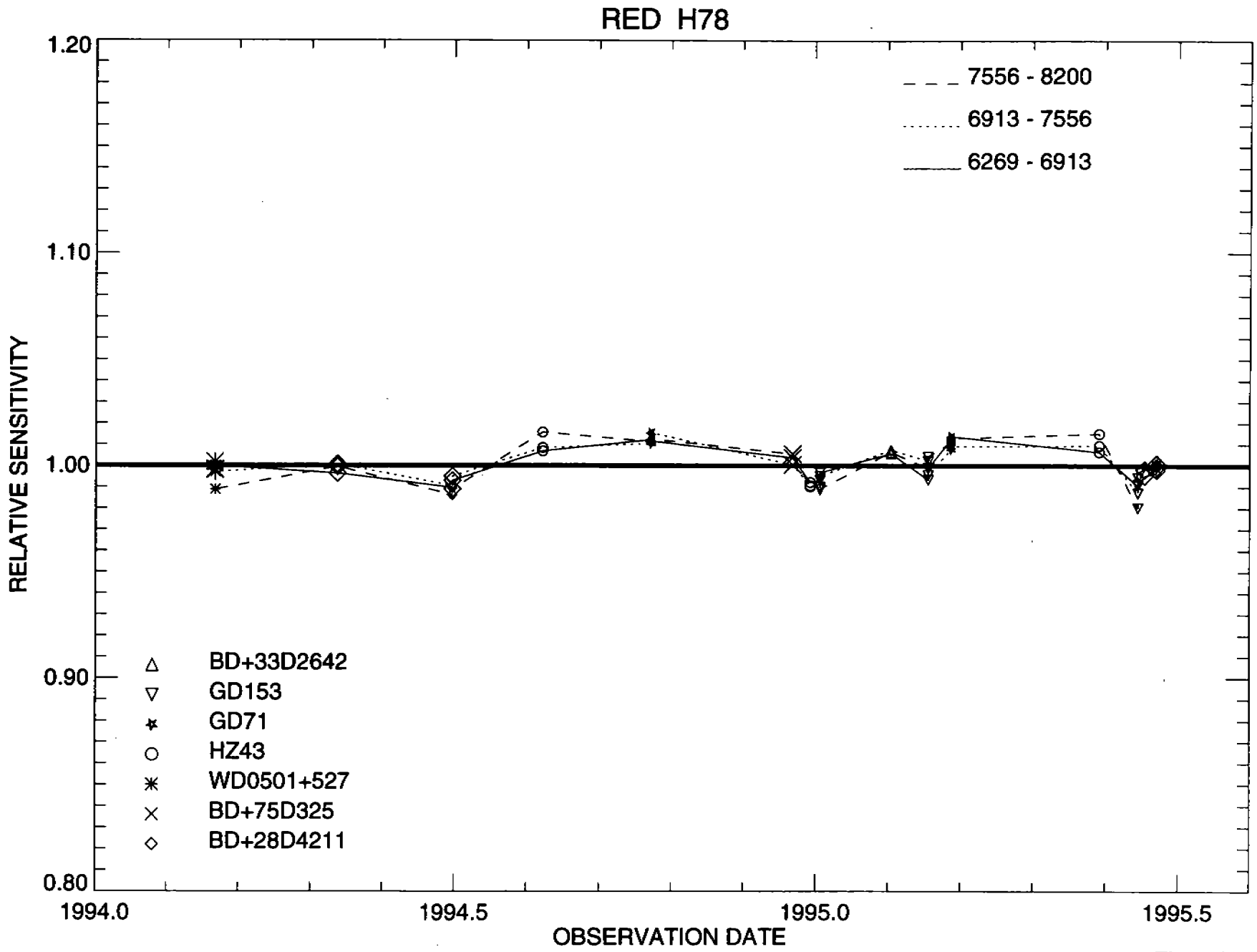

Fig. 2 (cont.)

LINDLER: PLTSENS_TIME 25-Jul-1995 11:23

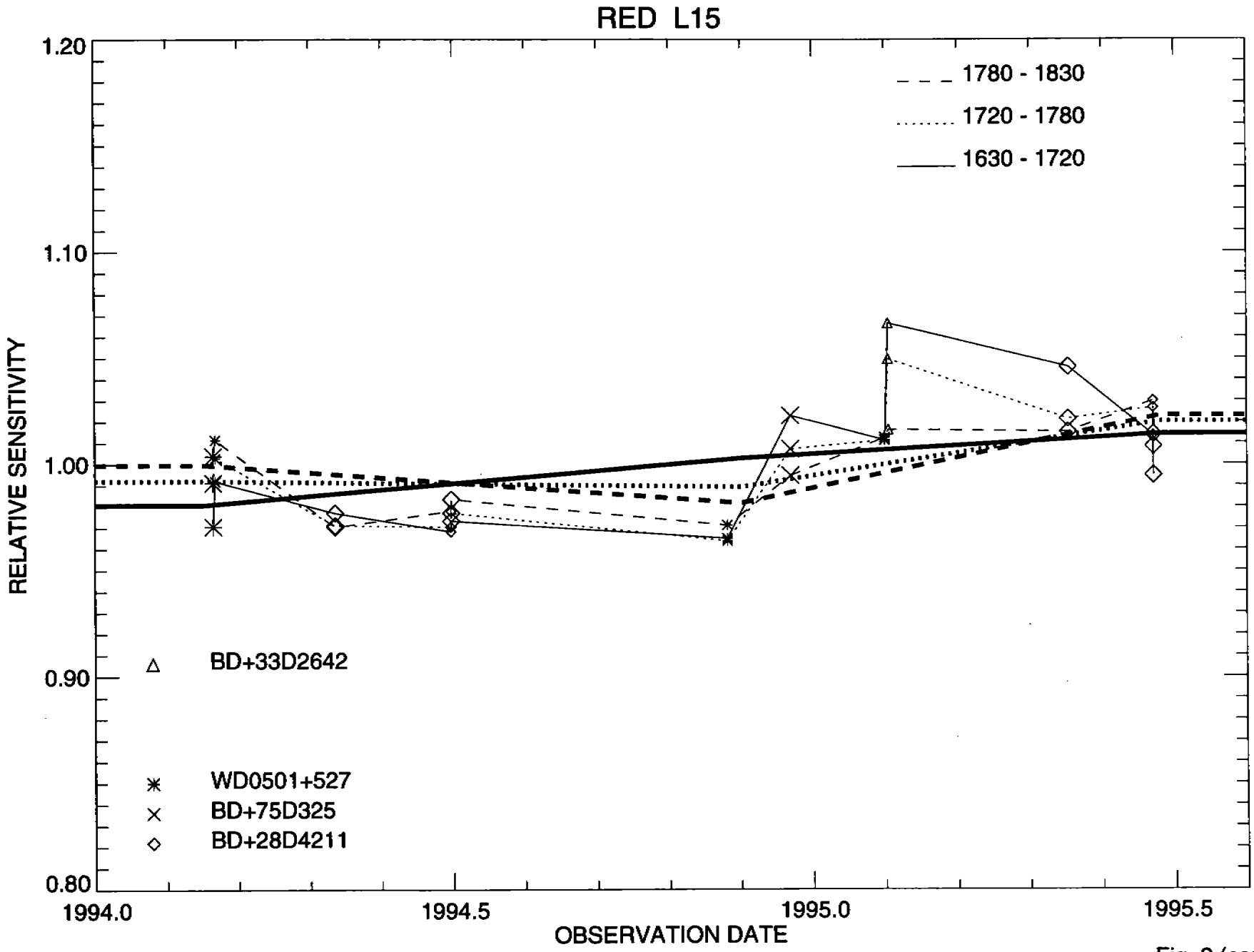

Fig. 2 (cont.)

LINDLER: PLTSENS_TIME 2[illegible]1995 11:24

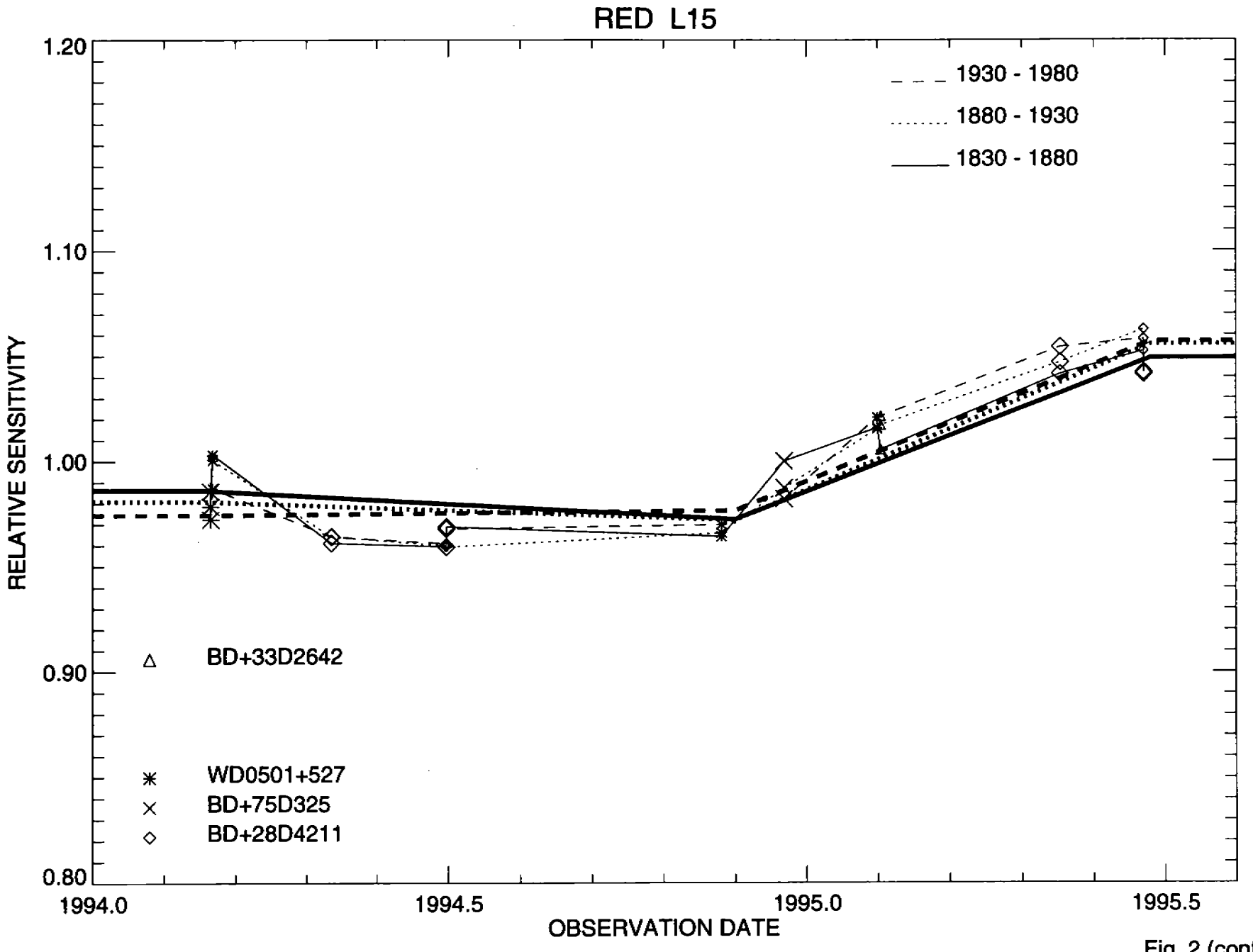

Fig. 2 (cont.)

UNDLER: PLTSENS_TIME 25-Jul-1995 11:24

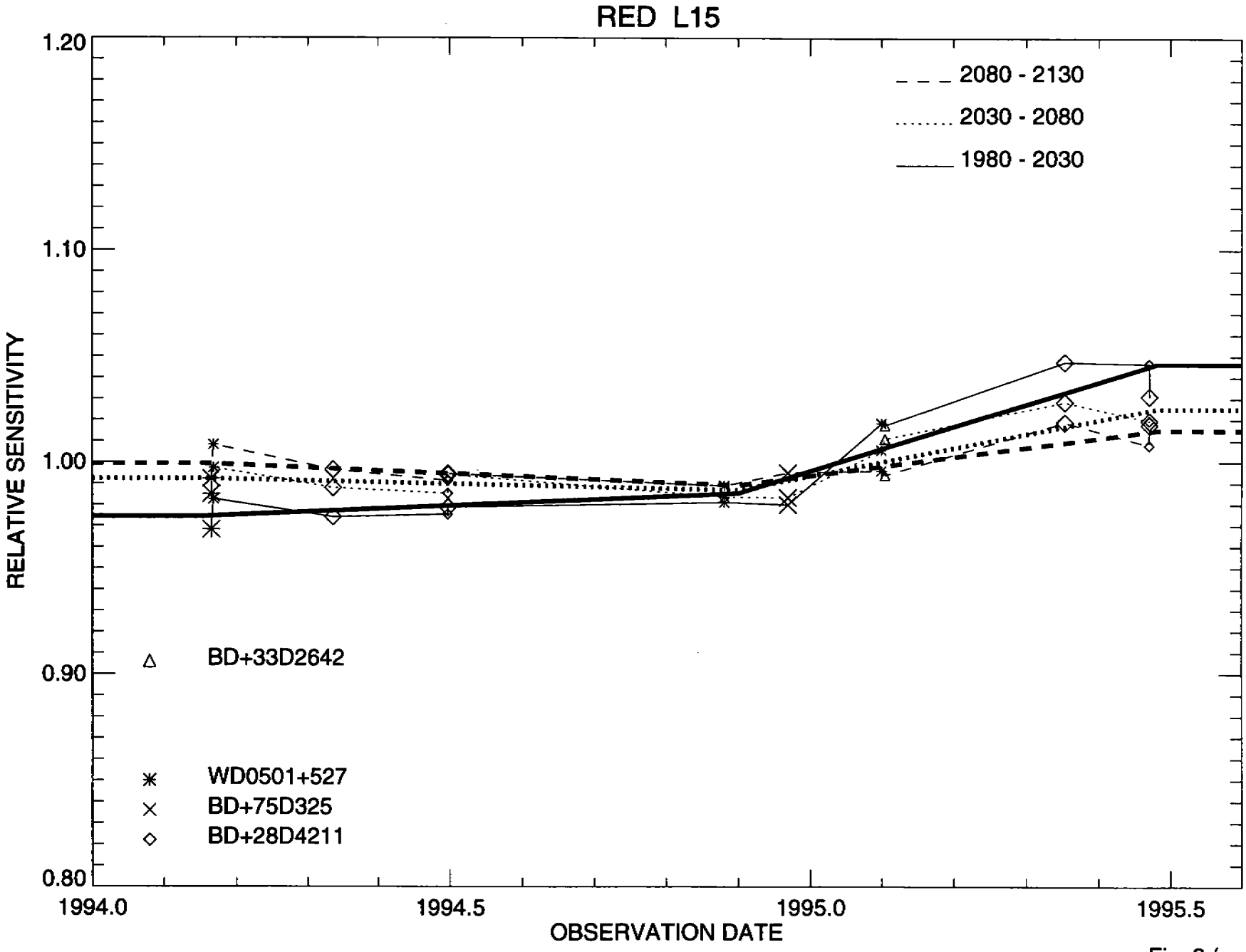

Fig. 2 (cont.)

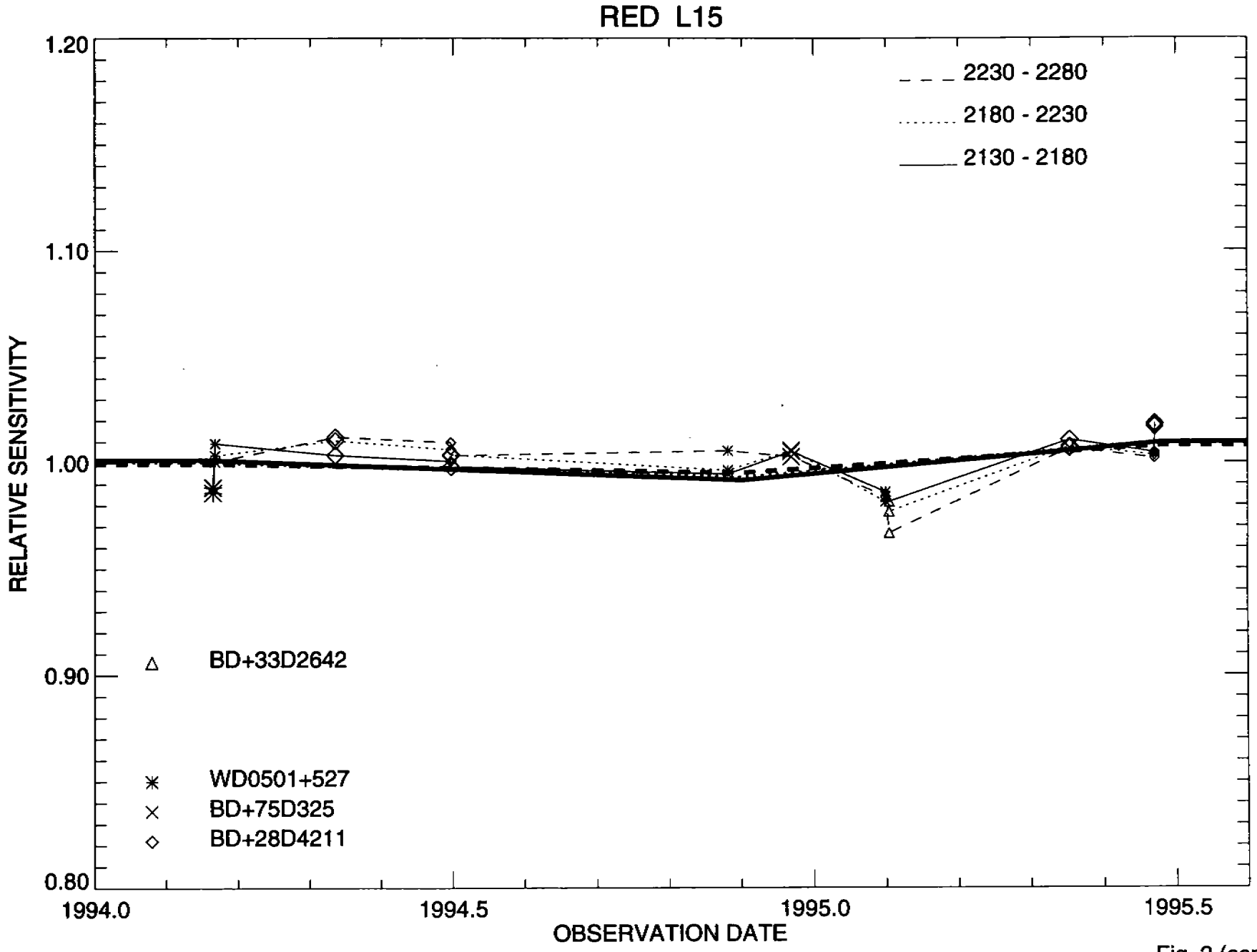

Fig. 2 (cont.)

LINDLER: PLTSENS_TIME 25-Jul-1995 11:24

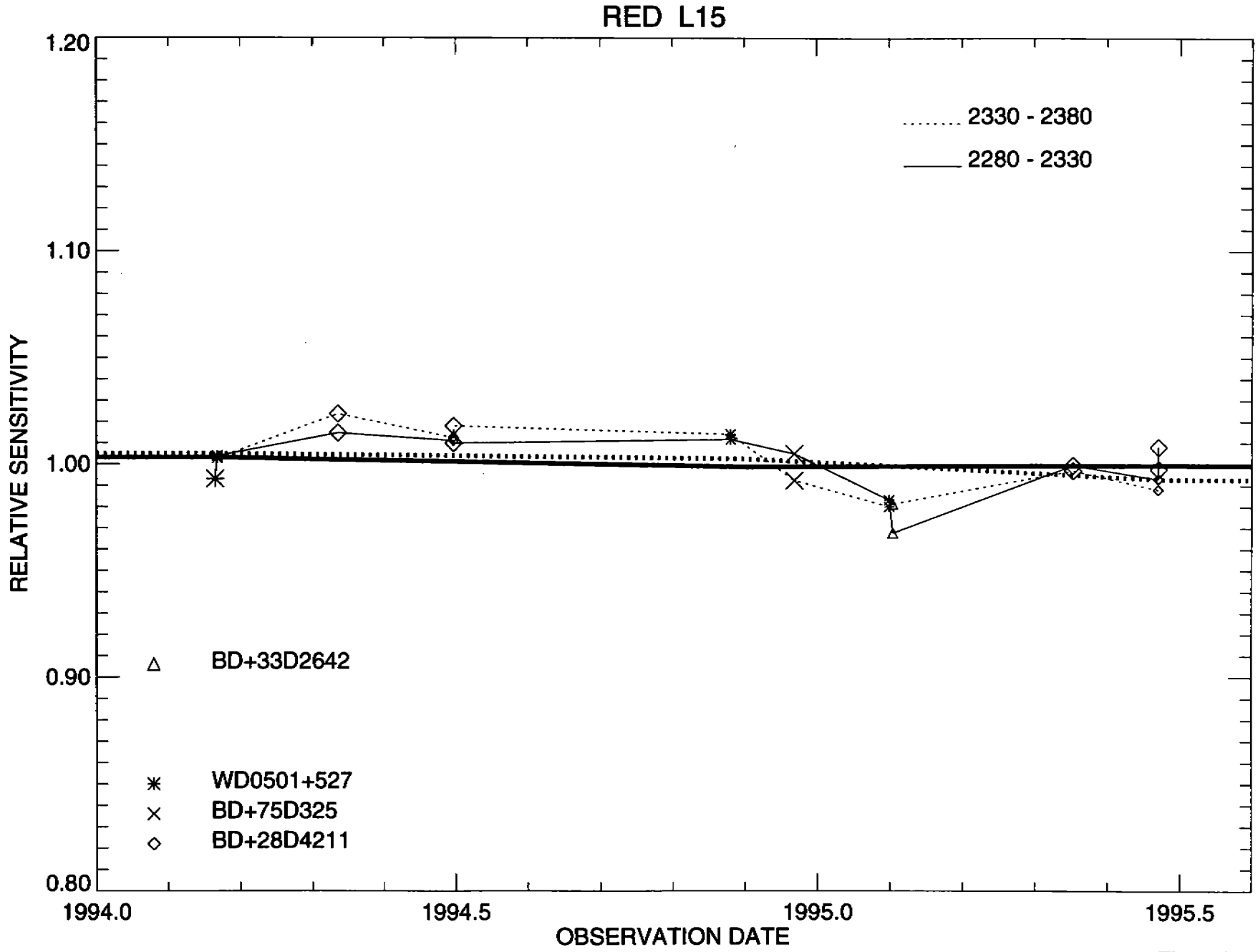

Fig. 2 (cont.)

LINDLER: PLTSENS_TIME 2 1995 11:24

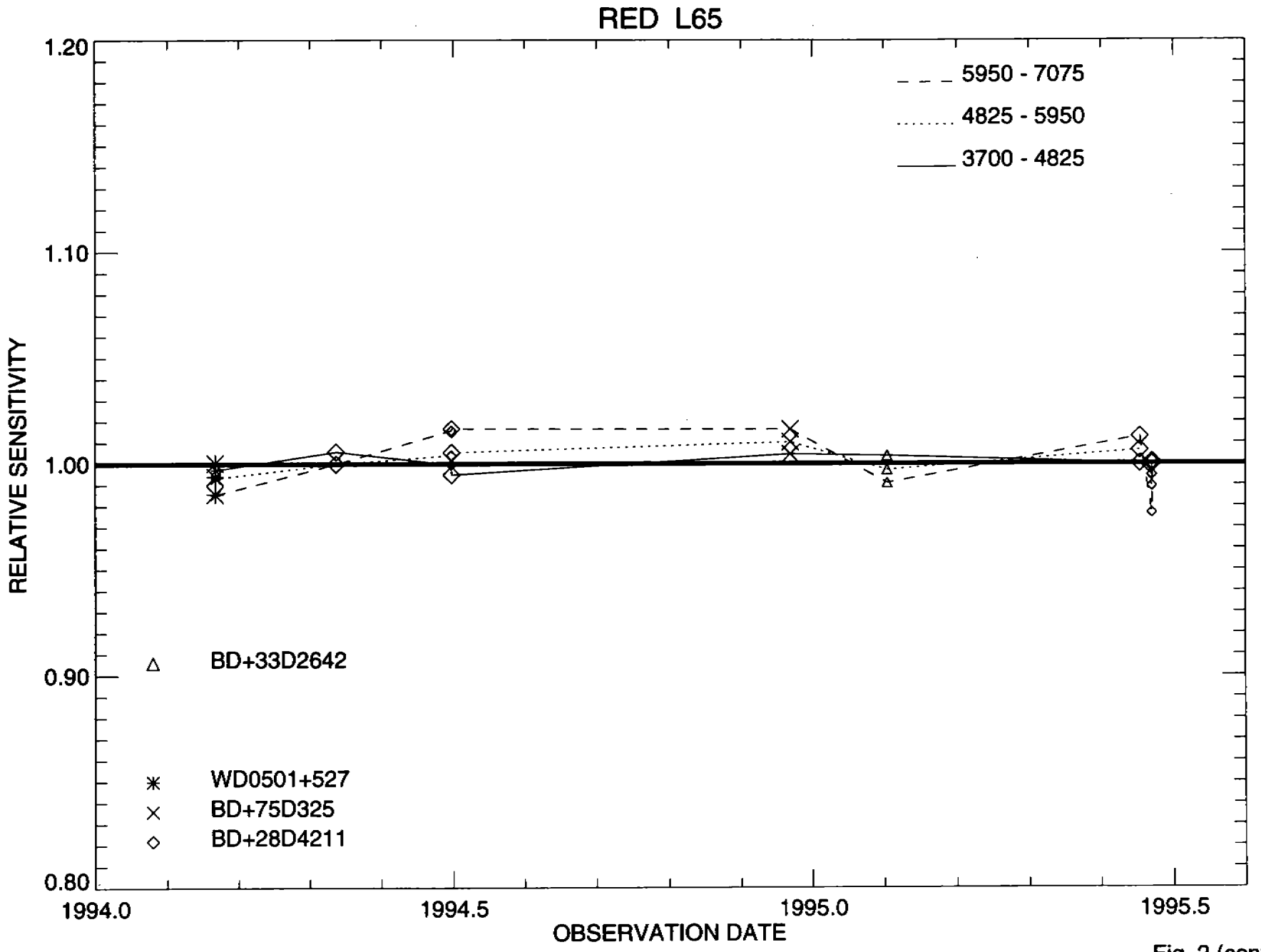

Fig. 2 (cont.)

LINDLER: PLTSENS_TIME 25-Jul-1995 11:24

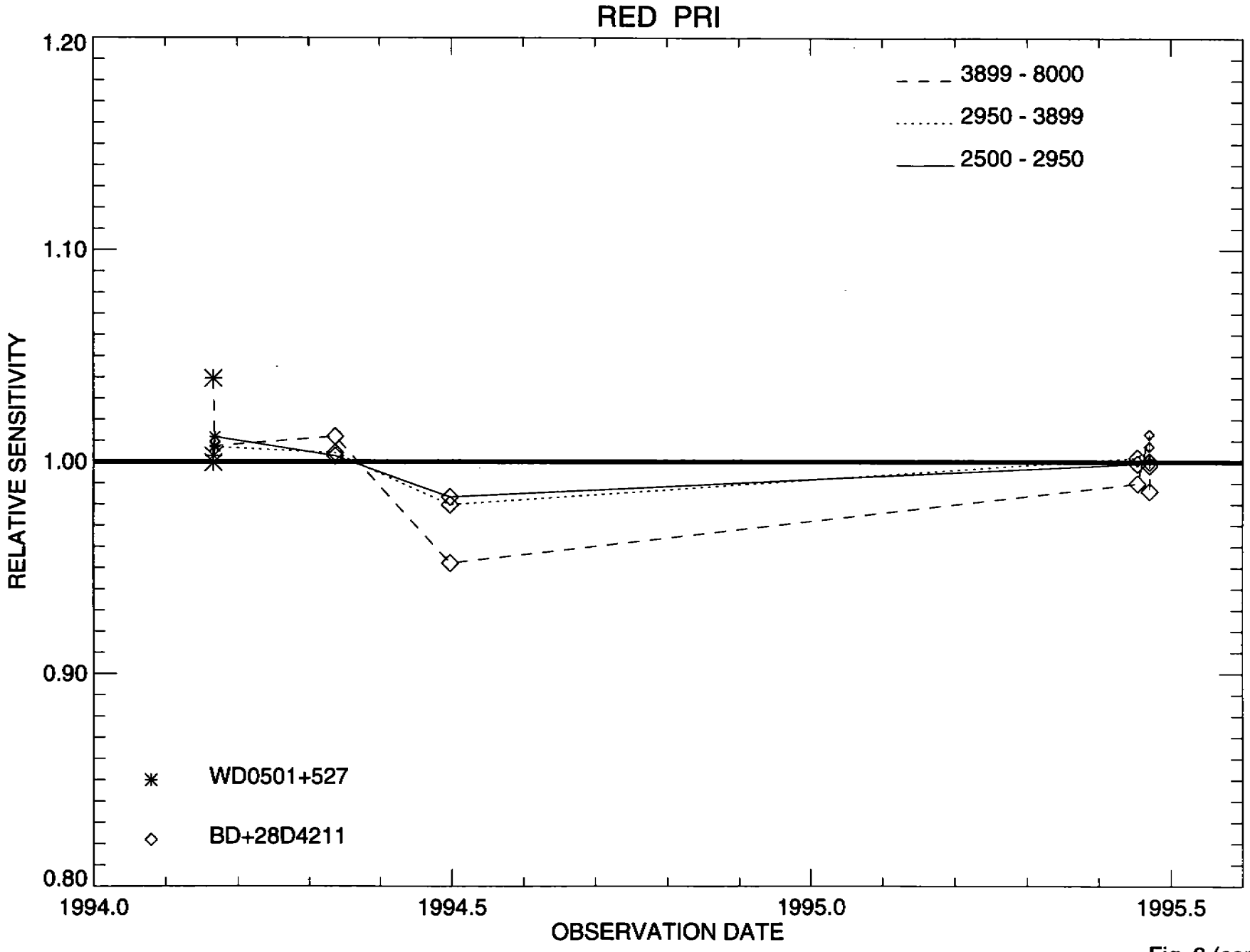

Fig. 2 (cont.)

LINDLER: PLTSENS_TIME 2[illegible]995 11:24

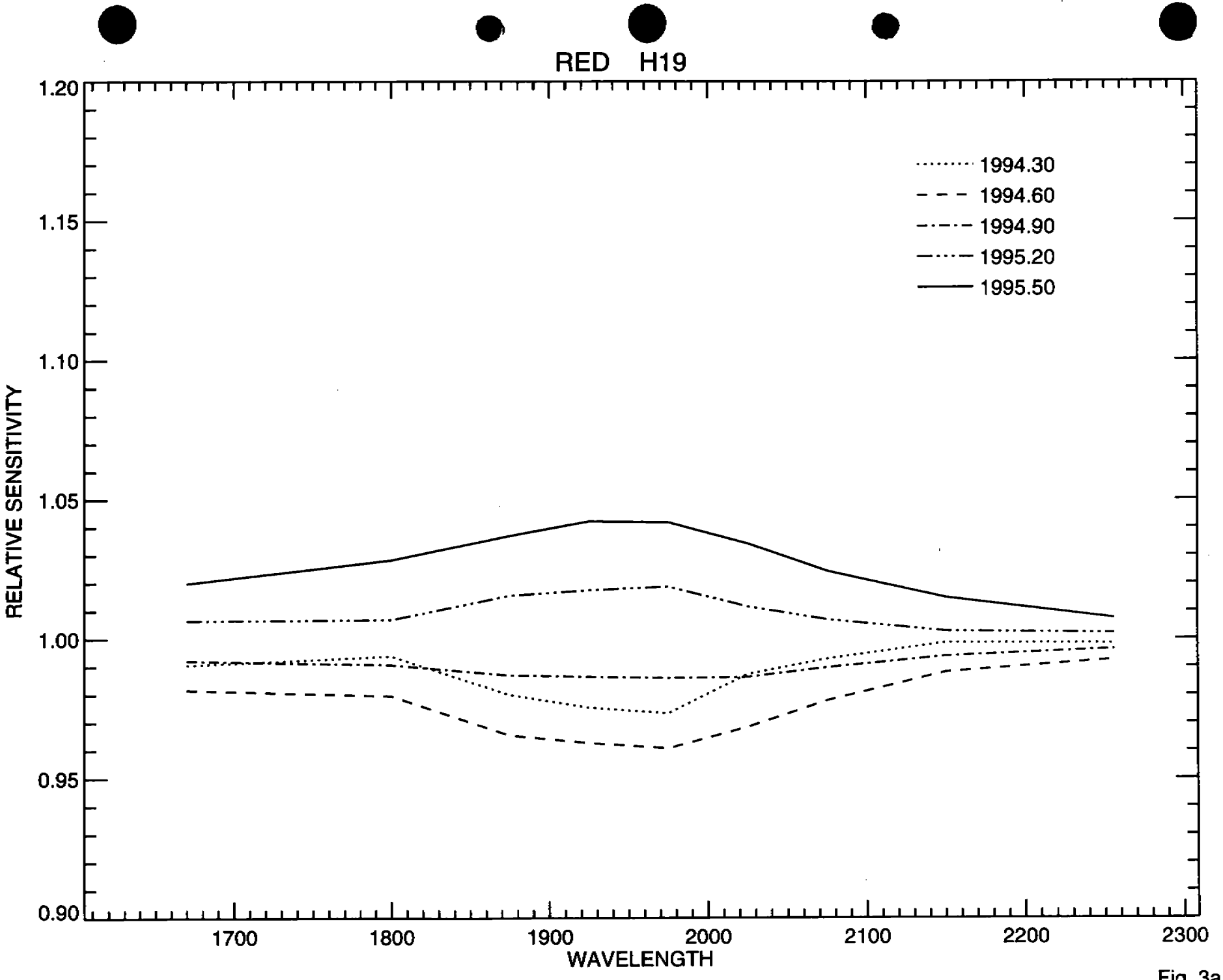
RED H19
1.20
1.15
1.10
1.05
1.00
0.95
0.90
RELATIVE SENSITIVITY
1994.30
1994.60
1994.90
1995.20
1995.50
1700
1800
1900
2000
2100
2200
2300
WAVELENGTH

Fig. 3a

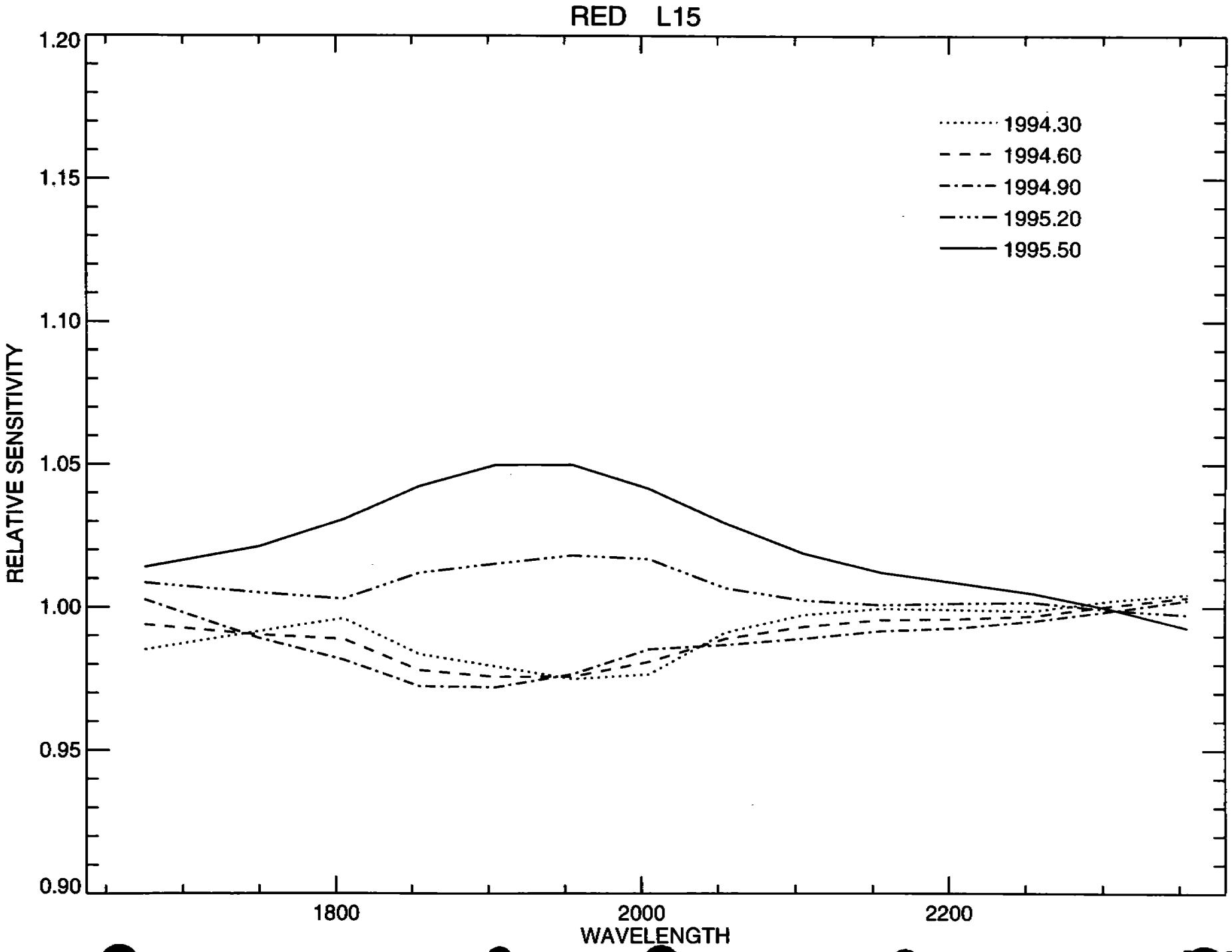
RED L15
1.20
1.15
1.10
1.05
1.00
0.95
0.90
RELATIVE SENSITIVITY
1800
2000
2200
WAVELENGTH
1994.30
1994.60
1994.90
1995.20
1995.50

Fig 3b

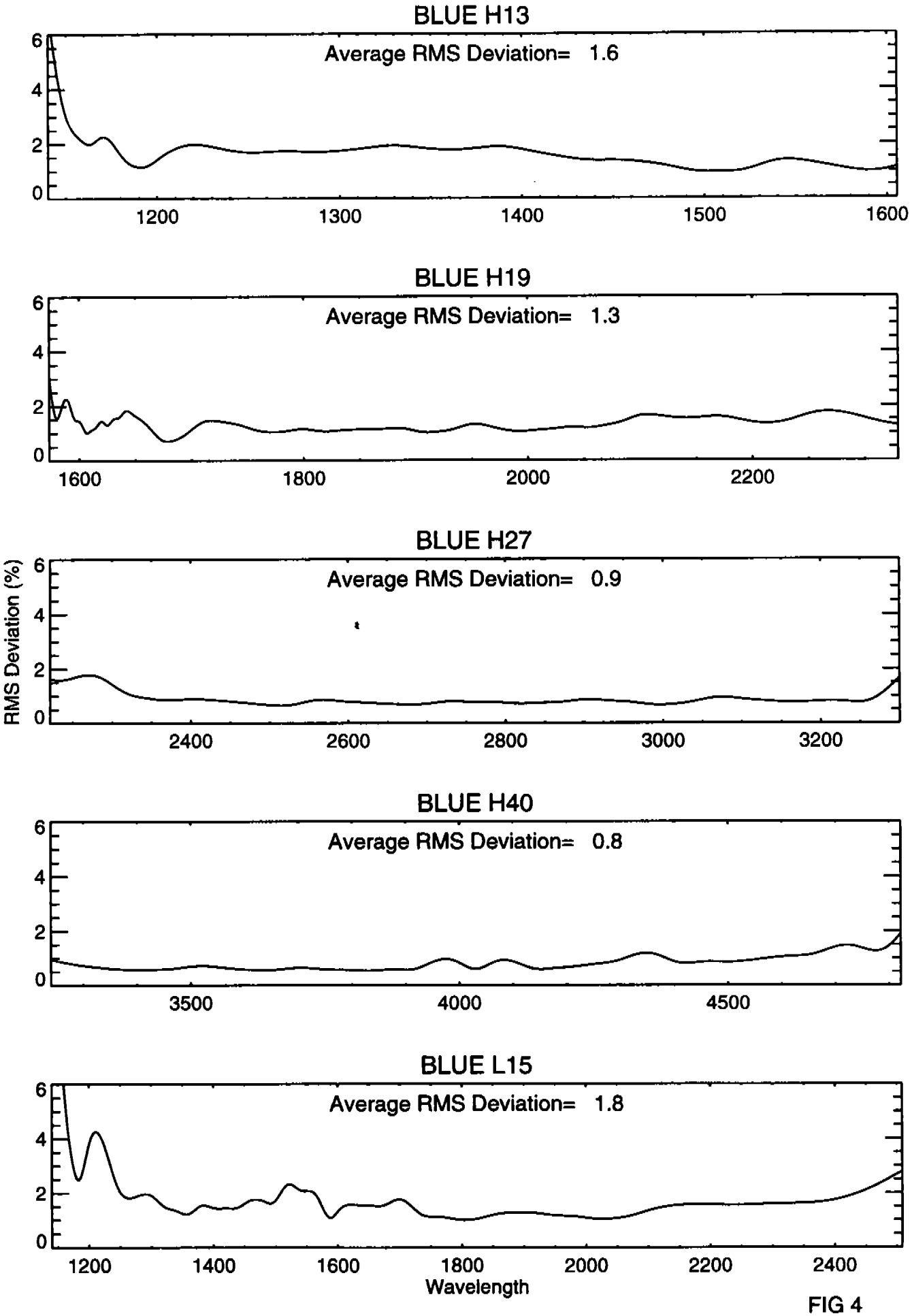

FIG 4

LINDLER: ave_ratio 25-Jul-1995 11:28

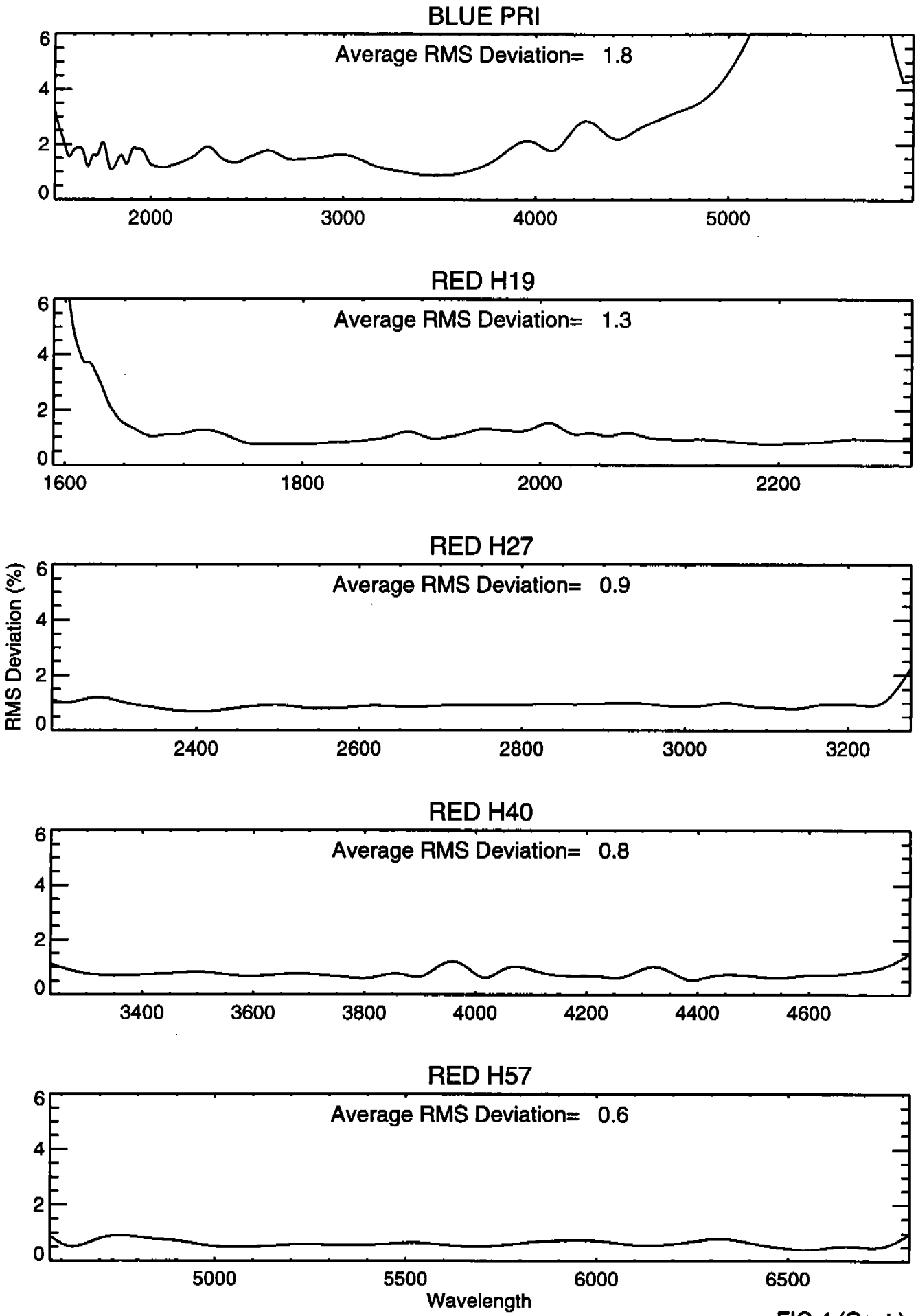

FIG 4 (Cont.)

LINDLER: ave_ratio 25-Jul-1995 11:26

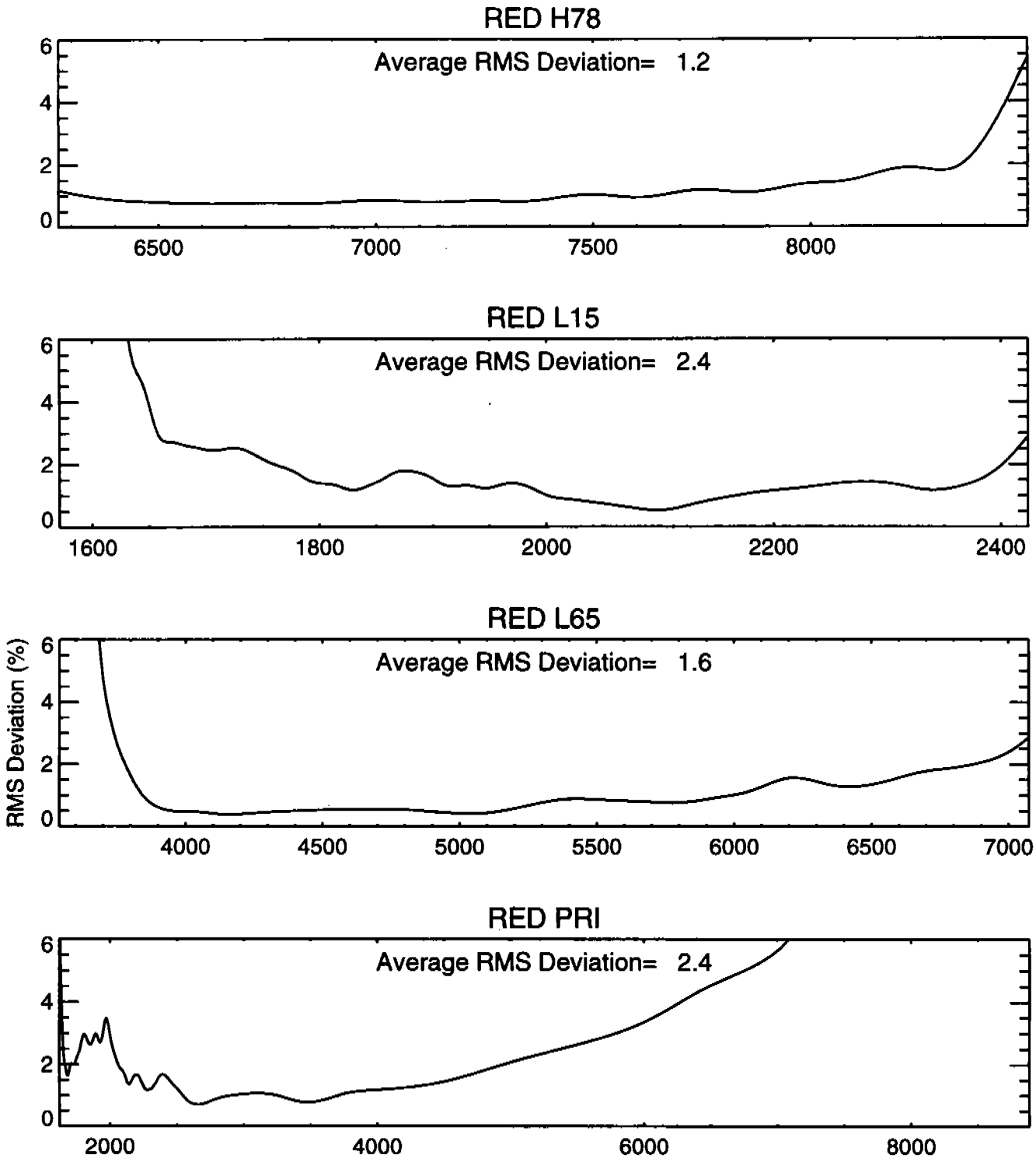

FIG 4 (Cont.)

LINDLER: ave_ratio 25-Jul-1995 11:26

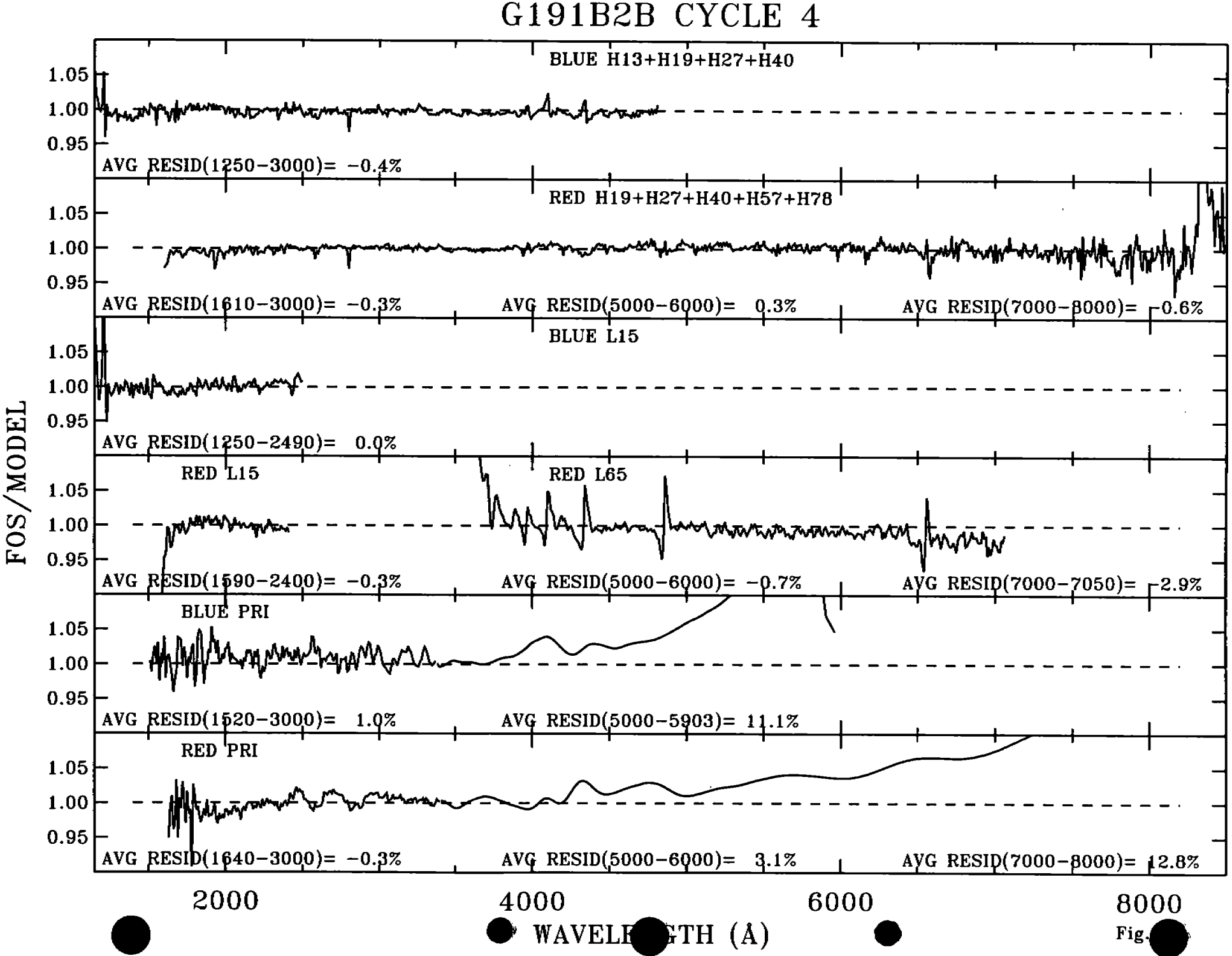
G191B2B CYCLE 4
BLUE H13+H19+H27+H40
AVG RESID(1250-3000)= -0.4%
RED H19+H27+H40+H57+H78
AVG RESID(1610-3000)= -0.3%
AVG RESID(5000-6000)= 0.3%
AVG RESID(7000-8000)= -0.6%
BLUE L15
AVG RESID(1250-2490)= 0.0%
RED L15
RED L65
AVG RESID(1590-2400)= -0.3%
AVG RESID(5000-6000)= -0.7%
AVG RESID(7000-7050)= -2.9%
BLUE PRI
AVG RESID(1520-3000)= 1.0%
AVG RESID(5000-5903)= 11.1%
RED PRI
AVG RESID(1640-3000)= -0.3%
AVG RESID(5000-6000)= 3.1%
AVG RESID(7000-8000)= 12.8%
1.05
1.00
0.95
FOS/MODEL
2000
4000
6000
8000
WAVELENGTH (Å)

Fig.

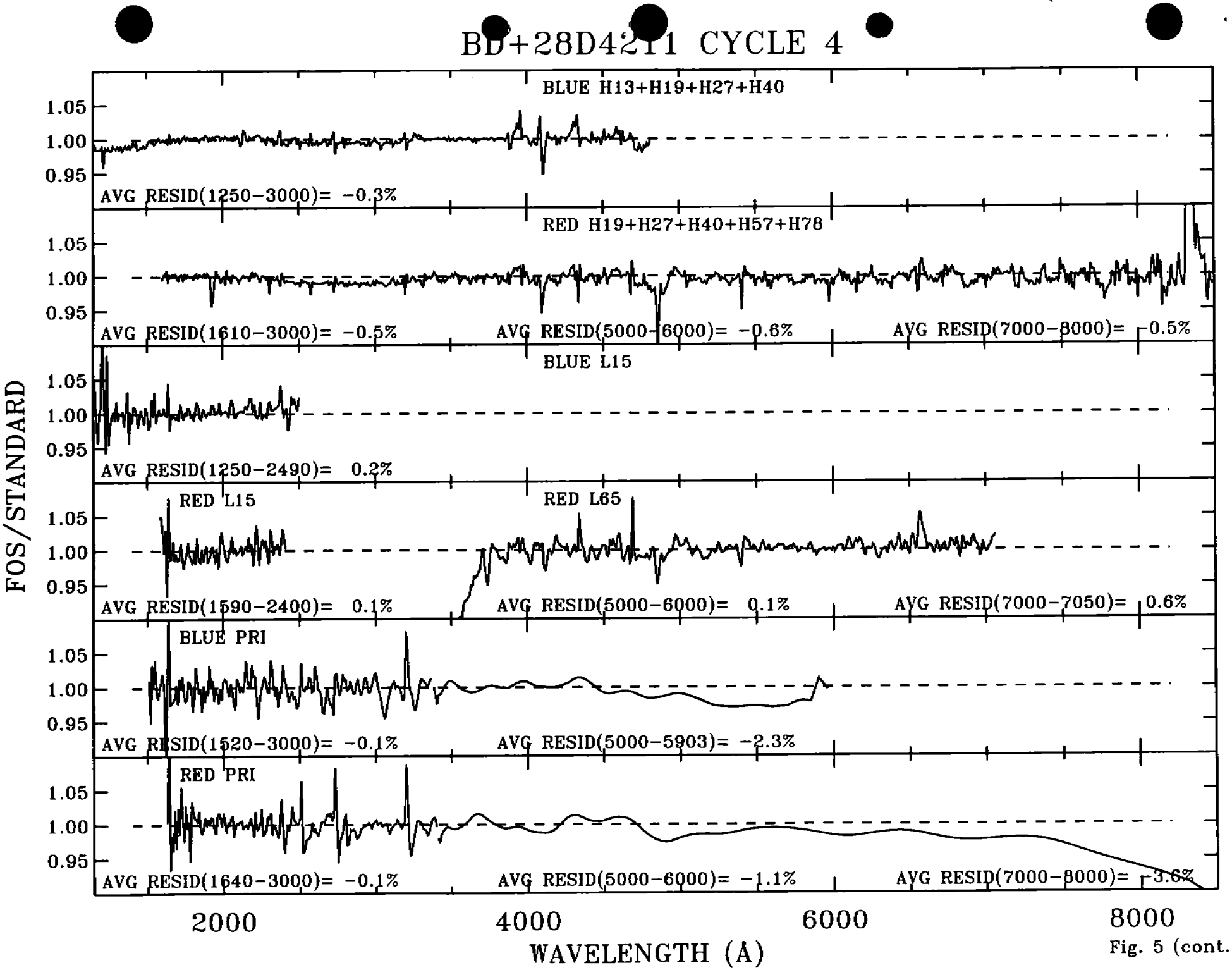
BD+28D4211 CYCLE 4
BLUE H13+H19+H27+H40
AVG RESID(1250-3000)= -0.3%
RED H19+H27+H40+H57+H78
AVG RESID(1610-3000)= -0.5%
AVG RESID(5000-6000)= -0.6%
AVG RESID(7000-8000)= -0.5%
BLUE L15
AVG RESID(1250-2490)= 0.2%
RED L15
RED L65
AVG RESID(1590-2400)= 0.1%
AVG RESID(5000-6000)= 0.1%
AVG RESID(7000-7050)= 0.6%
BLUE PRI
AVG RESID(1520-3000)= -0.1%
AVG RESID(5000-5903)= -2.3%
RED PRI
AVG RESID(1640-3000)= -0.1%
AVG RESID(5000-6000)= -1.1%
AVG RESID(7000-8000)= -3.6%
FOS/STANDARD
1.05
1.00
0.95
2000
4000
6000
8000
WAVELENGTH (A)

Fig. 5 (cont.)

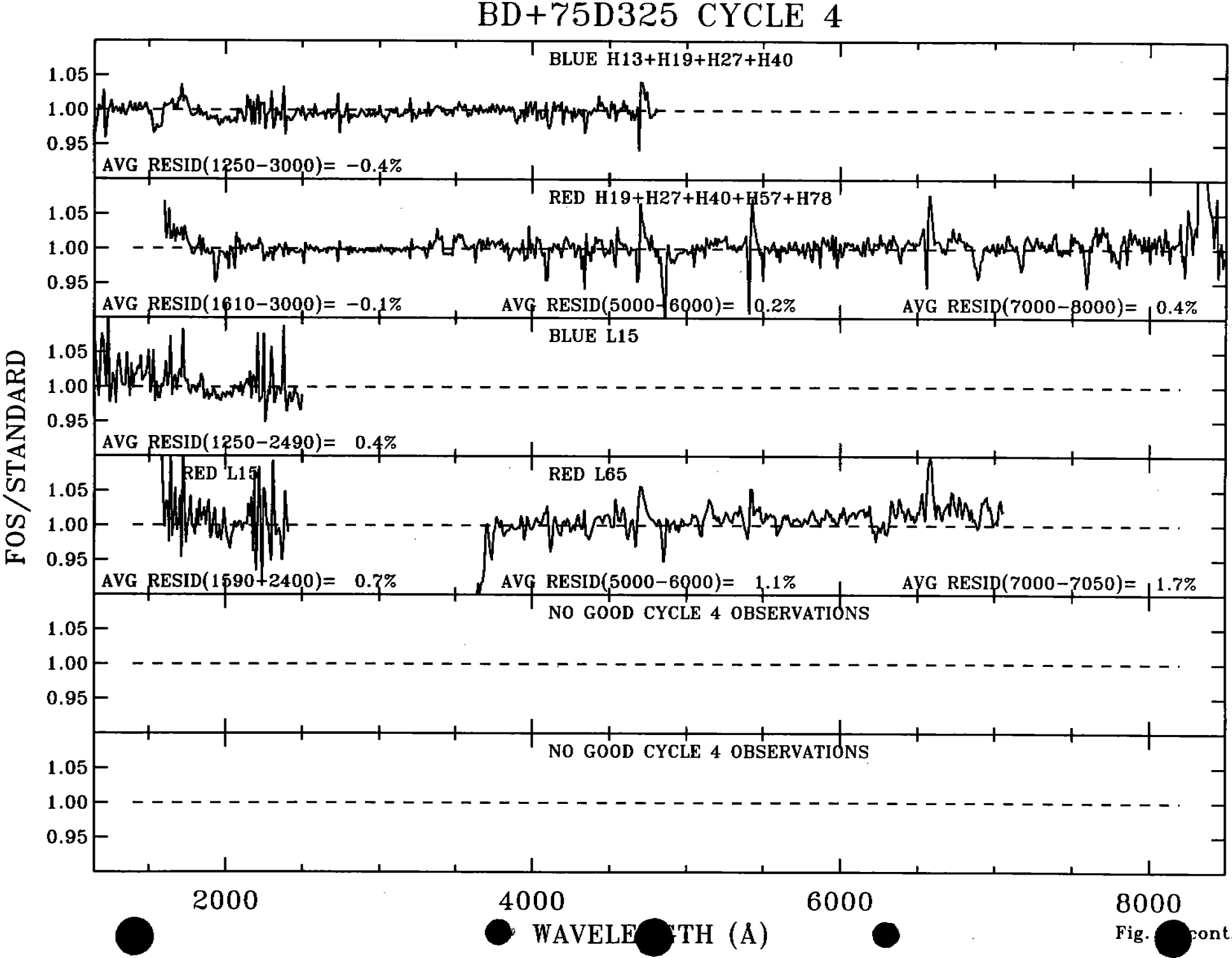
BD+75D325 CYCLE 4
BLUE H13+H19+H27+H40
AVG RESID(1250-3000)= -0.4%
RED H19+H27+H40+H57+H78
AVG RESID(1610-3000)= -0.1%
AVG RESID(5000-6000)= 0.2%
AVG RESID(7000-8000)= 0.4%
BLUE L15
AVG RESID(1250-2490)= 0.4%
RED L15
RED L65
AVG RESID(1590-2400)= 0.7%
AVG RESID(5000-6000)= 1.1%
AVG RESID(7000-7050)= 1.7%
NO GOOD CYCLE 4 OBSERVATIONS
NO GOOD CYCLE 4 OBSERVATIONS
FOS/STANDARD
1.05
1.00
0.95
2000
4000
6000
8000
WAVELENGTH (Å)

Fig. (cont.)

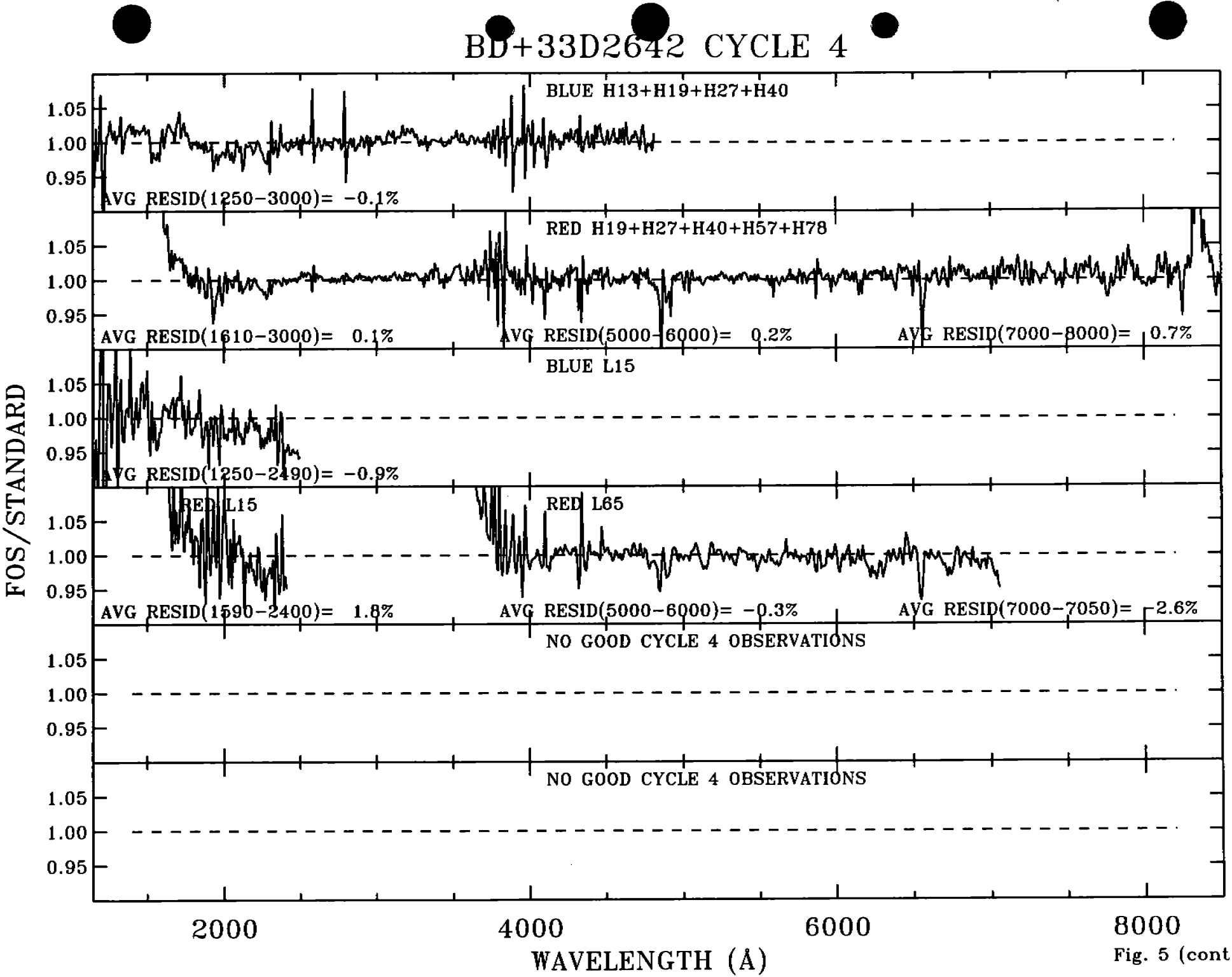
BD+33D2642 CYCLE 4
BLUE H13+H19+H27+H40
AVG RESID(1250-3000)= -0.1%
RED H19+H27+H40+H57+H78
AVG RESID(1610-3000)= 0.1%
AVG RESID(5000-6000)= 0.2%
AVG RESID(7000-8000)= 0.7%
BLUE L15
AVG RESID(1250-2490)= -0.9%
RED L15
RED L65
AVG RESID(1590-2400)= 1.8%
AVG RESID(5000-6000)= -0.3%
AVG RESID(7000-7050)= 2.6%
NO GOOD CYCLE 4 OBSERVATIONS
NO GOOD CYCLE 4 OBSERVATIONS
FOS/STANDARD
1.05
1.00
0.95
2000
4000
6000
8000
WAVELENGTH (Å)

Fig. 5 (cont.)

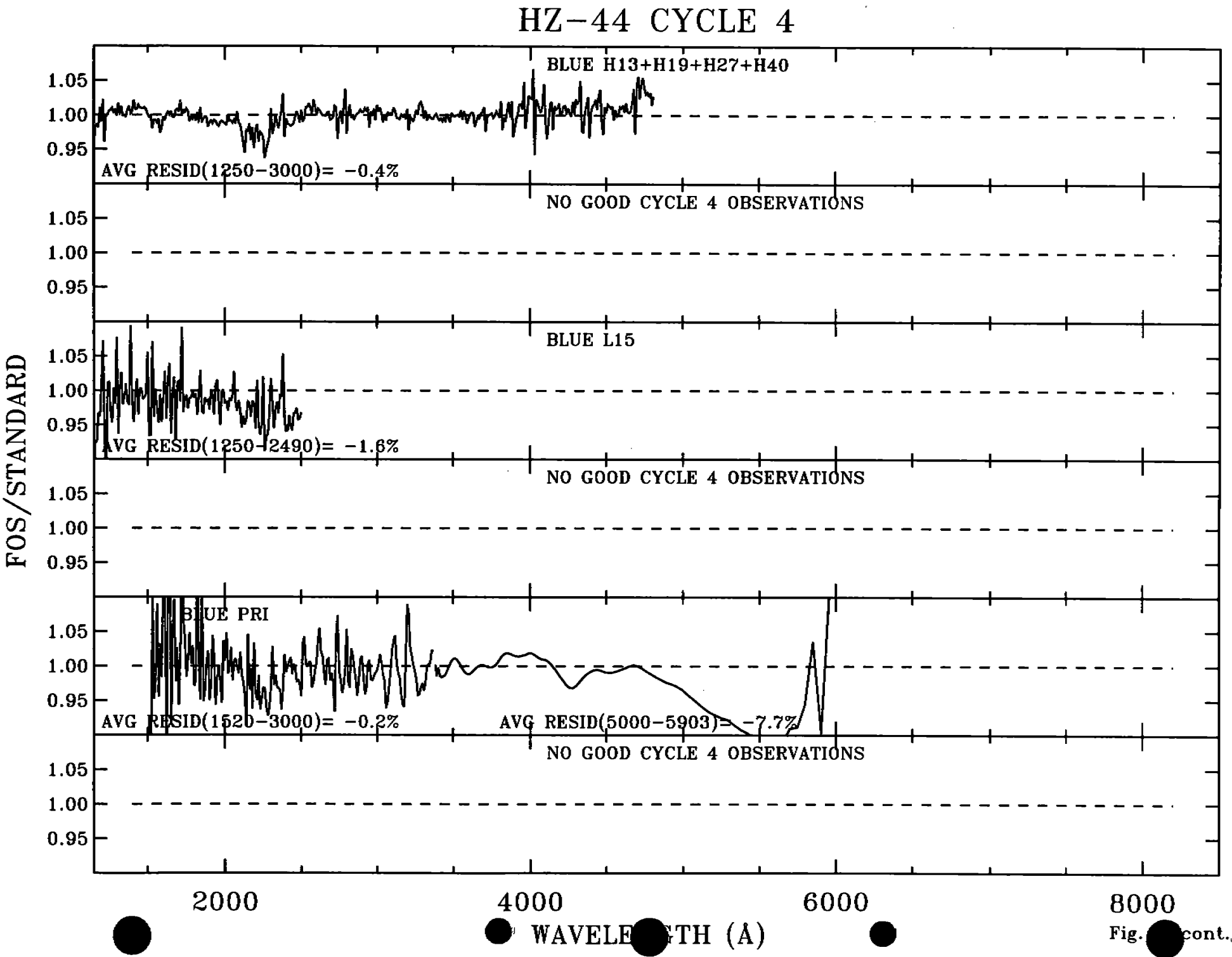
HZ−44 CYCLE 4
BLUE H13+H19+H27+H40
AVG RESID(1250−3000)= −0.4%
NO GOOD CYCLE 4 OBSERVATIONS
BLUE L15
AVG RESID(1250−2490)= −1.6%
NO GOOD CYCLE 4 OBSERVATIONS
BLUE PRI
AVG RESID(1520−3000)= −0.2%
AVG RESID(5000−5903)= −7.7%
NO GOOD CYCLE 4 OBSERVATIONS
FOS/STANDARD
1.05
1.00
0.95
2000
4000
6000
8000
WAVELENGTH (Å)

Fig. (cont.)

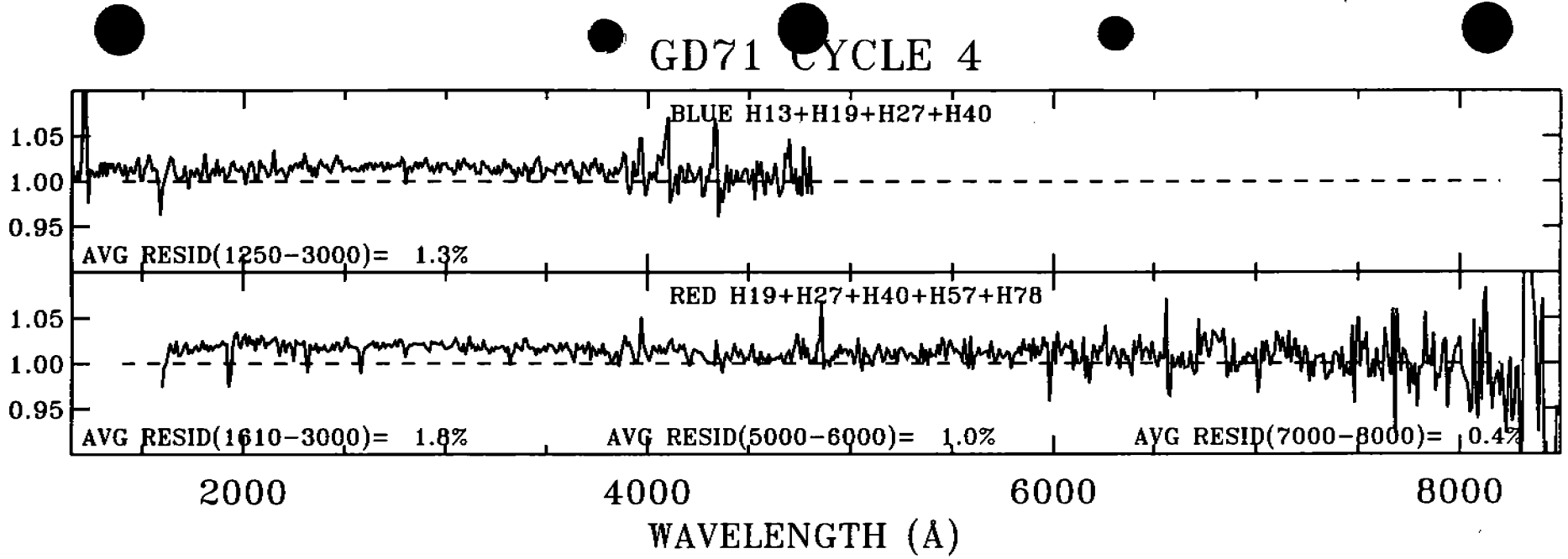
GD71 CYCLE 4
BLUE H13+H19+H27+H40
1.05
1.00
0.95
AVG RESID(1250-3000)= 1.3%
RED H19+H27+H40+H57+H78
1.05
1.00
0.95
AVG RESID(1610-3000)= 1.8%
AVG RESID(5000-6000)= 1.0%
AVG RESID(7000-8000)= 0.4%
2000
4000
6000
8000
WAVELENGTH (Å)
FOS/MODEL

Fig. 5 (cont.)

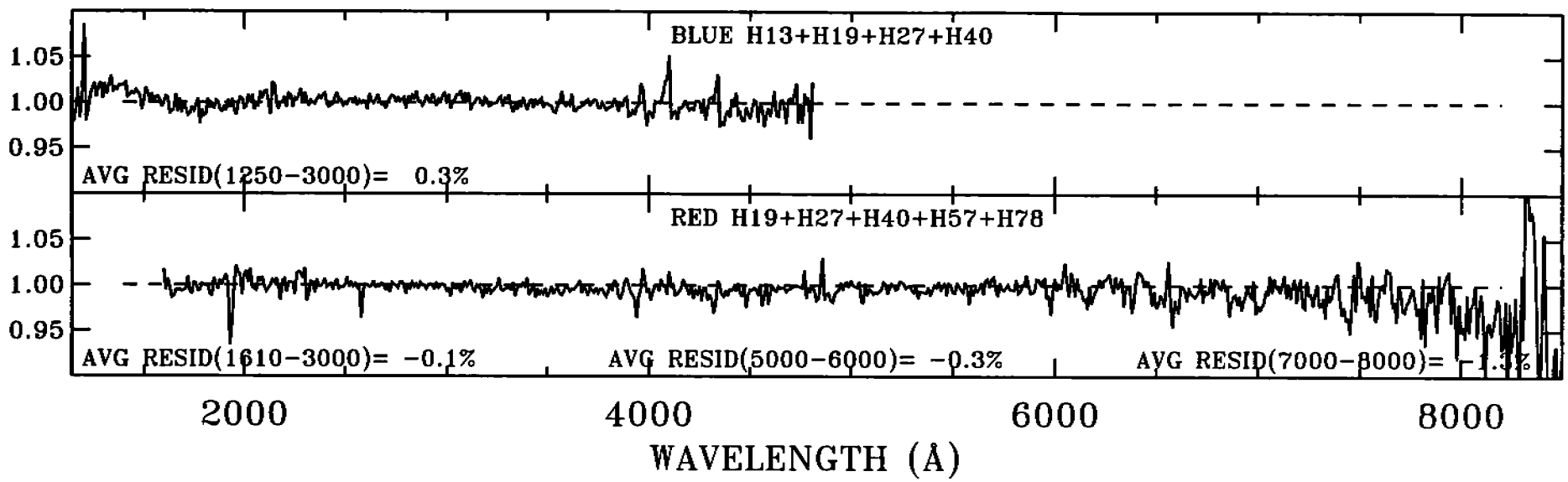
GD153 CYCLE 4
BLUE H13+H19+H27+H40
1.05
1.00
0.95
AVG RESID(1250-3000)= 0.3%
RED H19+H27+H40+H57+H78
1.05
1.00
0.95
AVG RESID(1610-3000)= -0.1%
AVG RESID(5000-6000)= -0.3%
AVG RESID(7000-8000)= -1.3%
2000
4000
6000
8000
WAVELENGTH (Å)
FOS/MODEL

F 5 (cont.)

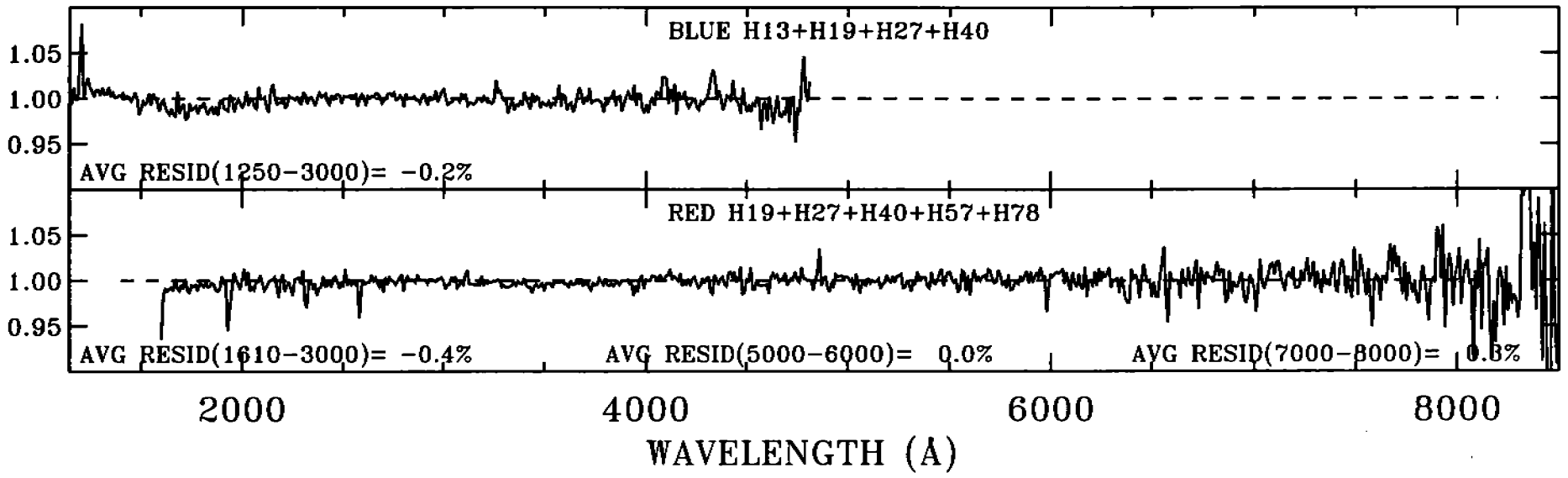
HZ43 CYCLE 4
BLUE H13+H19+H27+H40
1.05
1.00
0.95
AVG RESID(1250-3000)= -0.2%
RED H19+H27+H40+H57+H78
1.05
1.00
0.95
AVG RESID(1610-3000)= -0.4%
AVG RESID(5000-6000)= 0.0%
AVG RESID(7000-8000)= 0.3%
2000
4000
6000
8000
WAVELENGTH (Å)
FOS/MODEL

Fig. 5 (cont.)

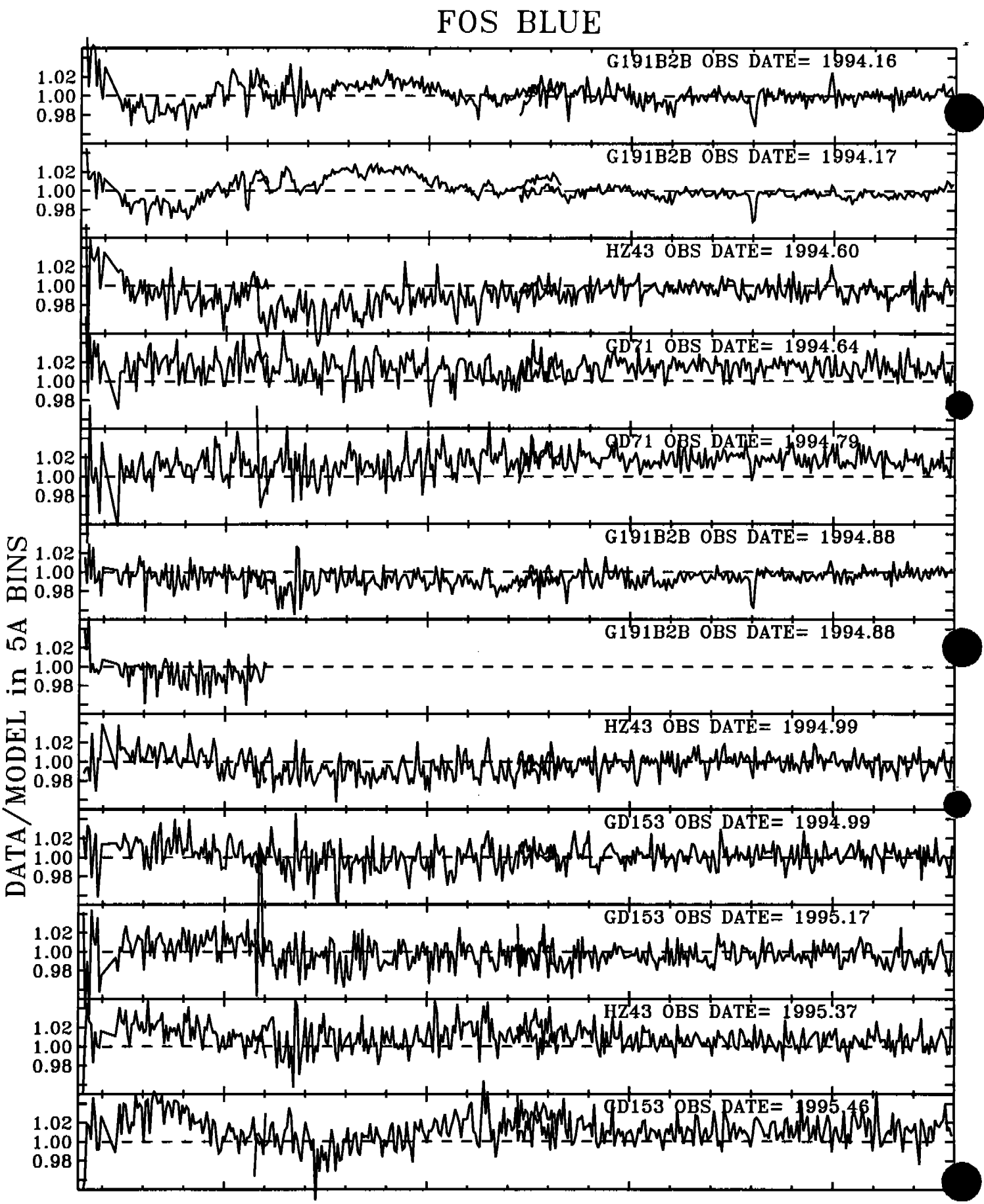

Fig. 6a

BOHLIN: WDSTACK 27-Jul-1995 14:32

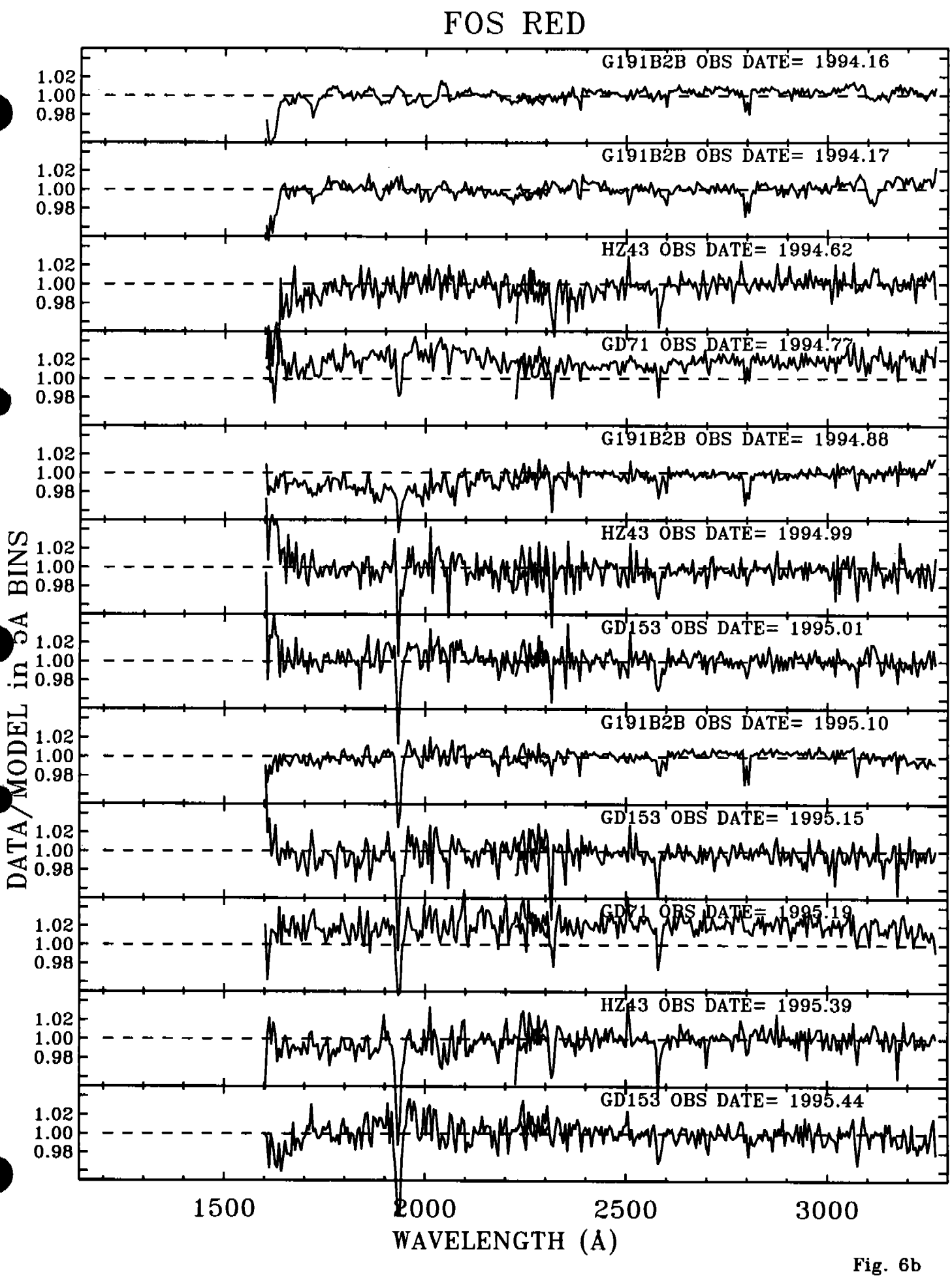

Fig. 6b

BOHLIN: WDSTACK 27-Jul-1995 14:34

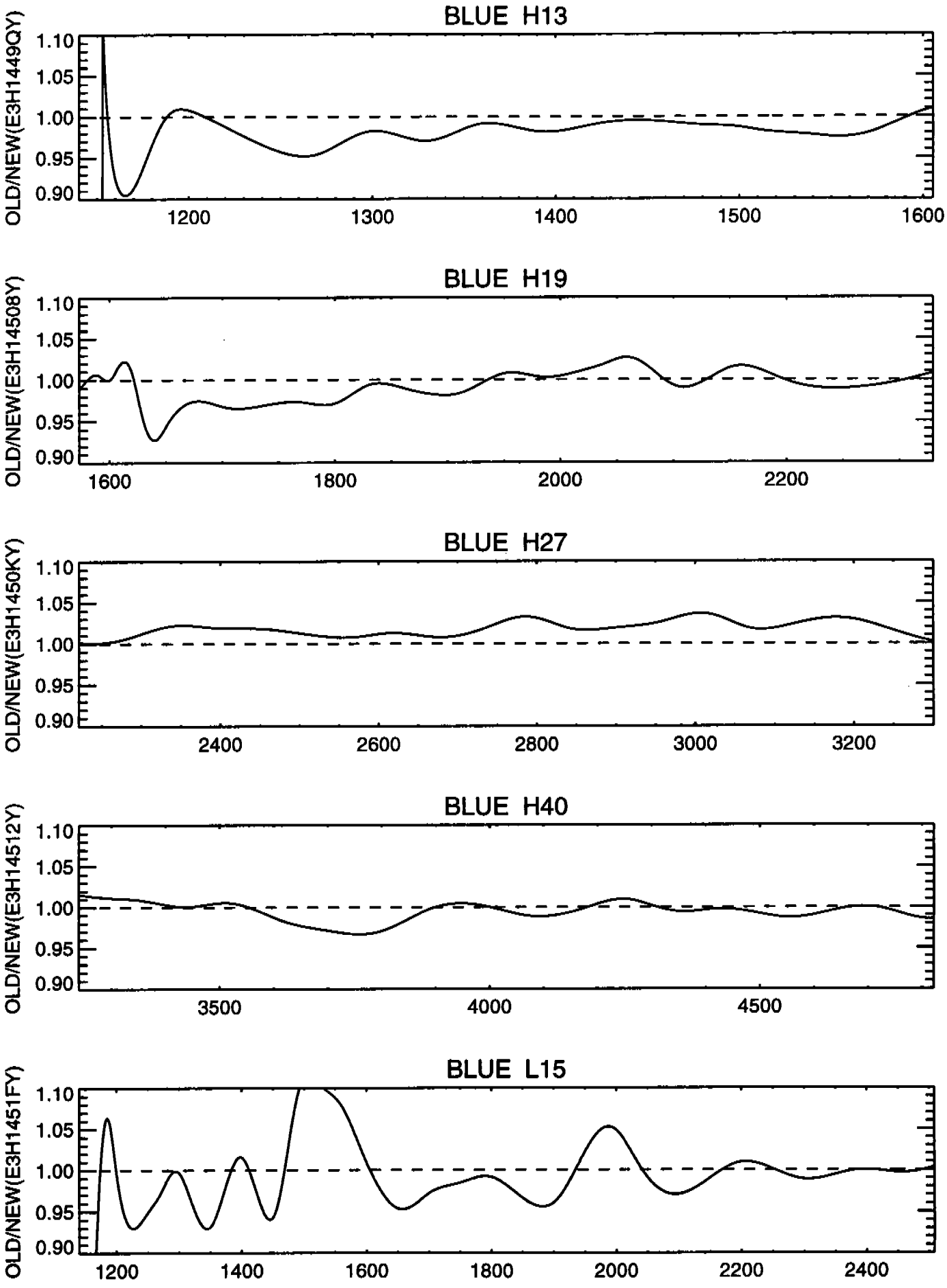
BLUE H13
OLD/NEW(E3H1449QY)
1.10
1.05
1.00
0.95
0.90
1200
1300
1400
1500
1600
BLUE H19
OLD/NEW(E3H14508Y)
1.10
1.05
1.00
0.95
0.90
1600
1800
2000
2200
BLUE H27
OLD/NEW(E3H1450KY)
1.10
1.05
1.00
0.95
0.90
2400
2600
2800
3000
3200
BLUE H40
OLD/NEW(E3H14512Y)
1.10
1.05
1.00
0.95
0.90
3500
4000
4500
BLUE L15
OLD/NEW(E3H1451FY)
1.10
1.05
1.00
0.95
0.90
1200
1400
1600
1800
2000
2200
2400

Fig. 7

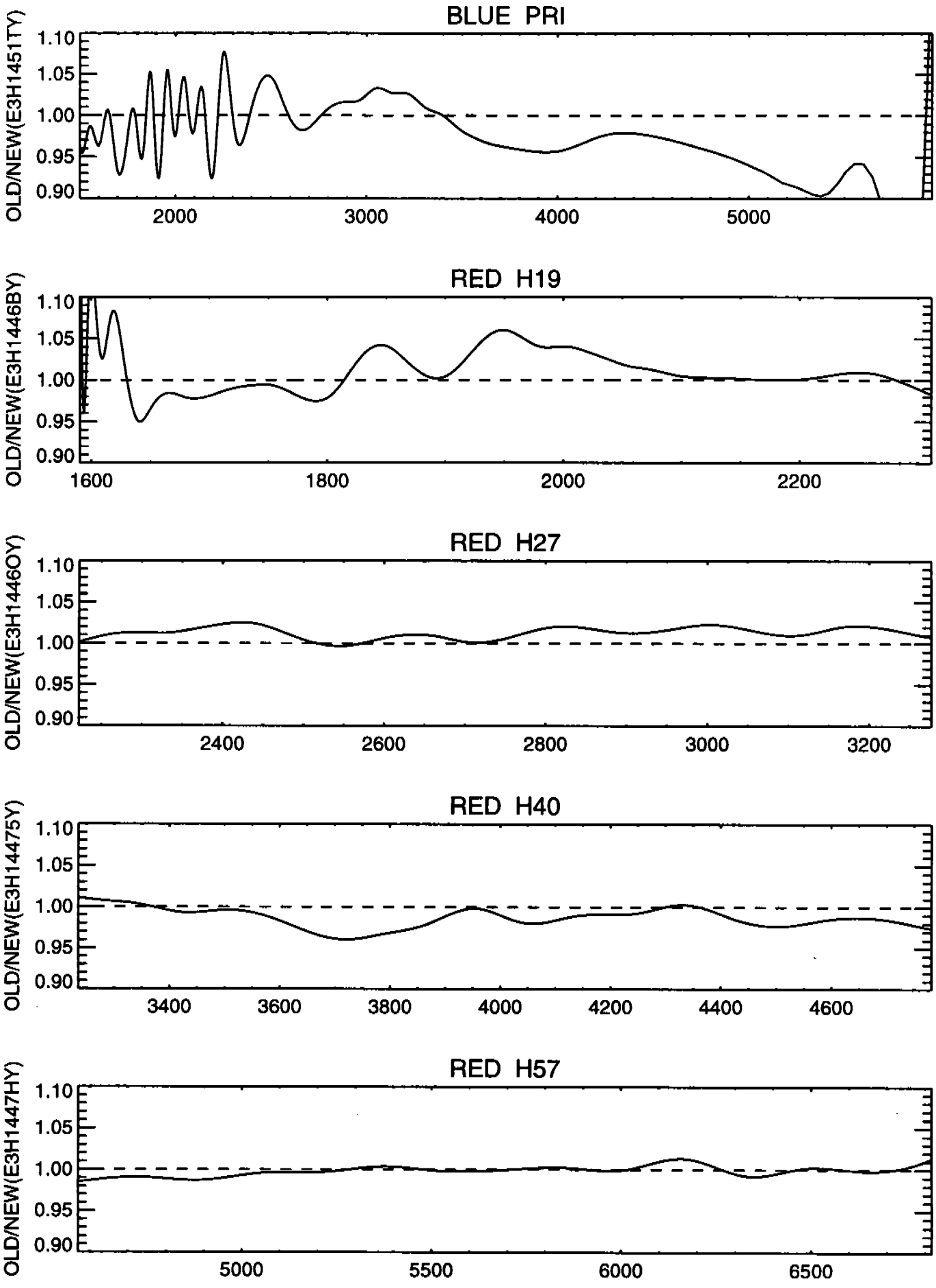
BLUE PRI
OLD/NEW(E3H1451TY)
1.10
1.05
1.00
0.95
0.90
2000
3000
4000
5000
RED H19
OLD/NEW(E3H1446BY)
1.10
1.05
1.00
0.95
0.90
1600
1800
2000
2200
RED H27
OLD/NEW(E3H1446OY)
1.10
1.05
1.00
0.95
0.90
2400
2600
2800
3000
3200
RED H40
OLD/NEW(E3H14475Y)
1.10
1.05
1.00
0.95
0.90
3400
3600
3800
4000
4200
4400
4600
RED H57
OLD/NEW(E3H1447HY)
1.10
1.05
1.00
0.95
0.90
5000
5500
6000
6500

Fig. 7 (cont.)

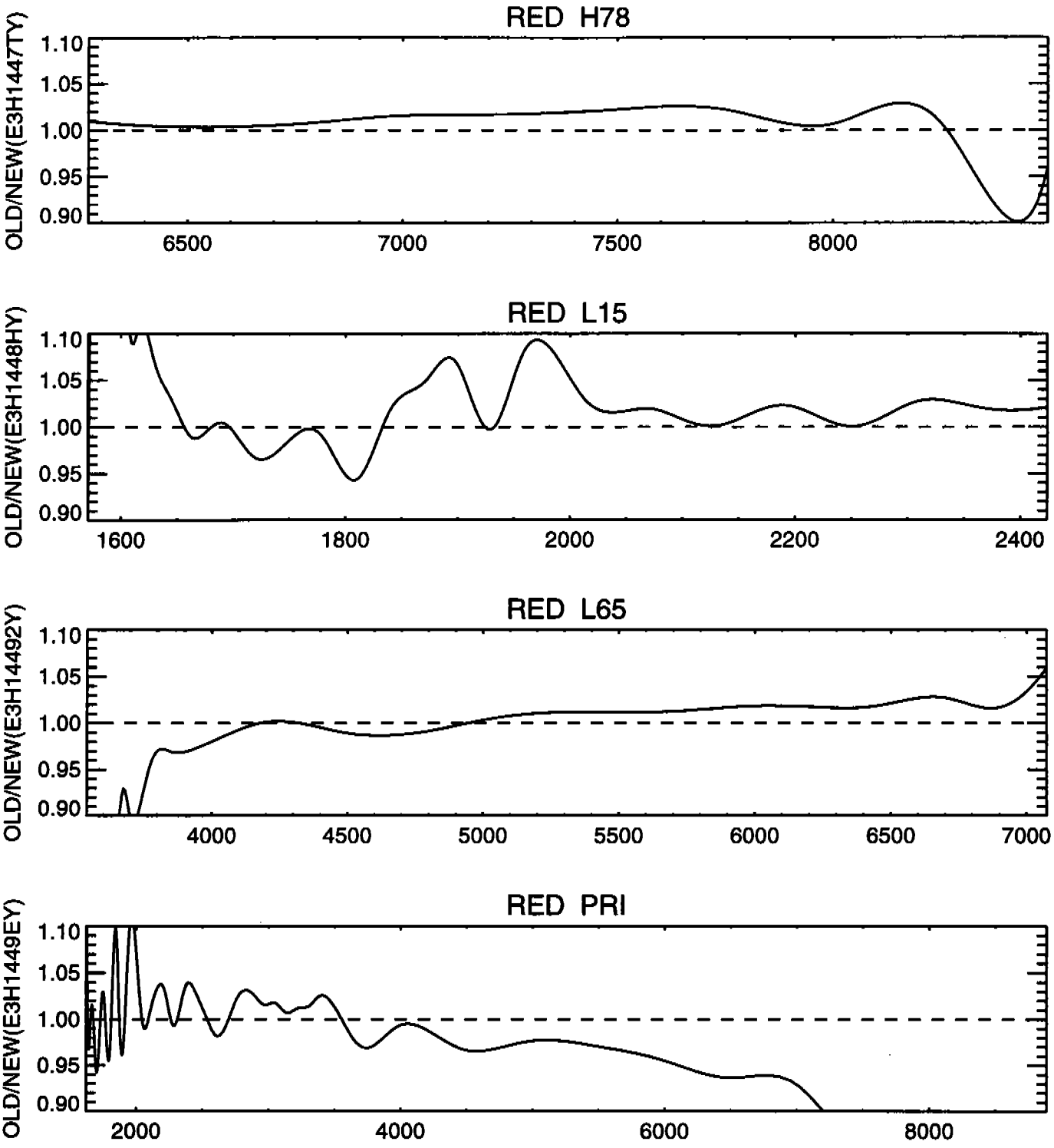
RED H78
OLD/NEW(E3H1447TY)
1.10
1.05
1.00
0.95
0.90
6500
7000
7500
8000
RED L15
OLD/NEW(E3H1448HY)
1.10
1.05
1.00
0.95
0.90
1600
1800
2000
2200
2400
RED L65
OLD/NEW(E3H14492Y)
1.10
1.05
1.00
0.95
0.90
4000
4500
5000
5500
6000
6500
7000
RED PRI
OLD/NEW(E3H1449EY)
1.10
1.05
1.00
0.95
0.90
2000
4000
6000
8000

Fig. 7 (cont.)